



Wall-Resolved Large-Eddy Simulations of Transonic Shock-Induced Flow Separation

Ali Uzun*

National Institute of Aerospace, Hampton, VA 23666

Mujeeb R. Malik†

NASA Langley Research Center, Hampton, VA 23681

Wall-resolved large-eddy simulations of shock-induced flow separation over an axisymmetric bump for a Mach number of 0.875 and a chord-based Reynolds number of 2.763 million are performed. The incoming boundary layer has a momentum-thickness Reynolds number of 6600 at 1.5 chords upstream of the bump. The calculations, which employ up to 24 billion grid points, simulate the experimental model of Bachalo and Johnson (*AIAA Journal*, Vol. 24, No. 3, 1986), except that the tunnel walls are ignored and free air is assumed. The effects of domain span and grid resolution are examined along with the main flowfield features. The predicted shock position as well as separation and reattachment locations agree well with the experiment. Grid convergence is observed in the attached region well upstream of separation. Two-point azimuthal correlations suggest that a span of at least 20 degrees is needed in the attached region, while a 120-degree span might be barely large enough in the separated region. Computed root-mean-square surface pressure fluctuations at the shock foot reach about 5 percent of ambient pressure and the level at the reattachment location drops to about half of the primary peak. Simulations reveal evidence of the low-frequency shock unsteadiness; however, a longer statistical sample is needed to investigate this phenomenon.

I. Introduction

Accurate prediction of smooth-body flow separation remains a subject of ongoing investigations because of its relevance to many technological applications. The turbulence research community is actively engaged in evaluating a number of computational strategies of varying degrees of fidelity for separated flows. Robust simulation tools that accurately predict flow separation in various configurations can help develop improved designs and control strategies to counteract the adverse effects of separation, such as increased aerodynamic drag, stall and reduced system performance. High Reynolds number separated flow problems are generally difficult to predict and have been mostly studied using techniques such as Reynolds-averaged Navier-Stokes (RANS) calculations, wall-modeled large-eddy simulations (WMLES) or hybrid RANS-LES type approaches. In the case of RANS, available turbulence models commonly fail to properly account for nonequilibrium effects in separated flows. An example demonstrating the failure of RANS in the well-known NASA wall-mounted hump test case can be found in the paper by Rumsey et al [1]. This commonly studied benchmark problem involves low-speed flow separation due to an adverse pressure gradient generated by a change in body contour in the aft portion of the hump. RANS has been found to significantly overpredict the separation-bubble length in this problem by as much as 35%, which is deemed unacceptable for design purposes. This failure of RANS has resulted in increased interest toward the use of scale-resolving approaches for the computation of separated flows. For example, for the NASA hump problem, WMLES studies by several groups [2–7] have reported generally better success than RANS but still exhibited some deficiencies in the overall skin-friction prediction, which is considered an important quantity of interest in aerodynamic design.

Although WMLES has seen recent widespread use in a number of problems, an important matter that has not been properly addressed by the community is the potential presence of multiple error sources in a typical WMLES calculation, in which the grid resolutions outside the wall-modeled region used by several researchers seem too coarse for LES. Outer grid spacings as large as a few hundred wall units along the streamwise and spanwise directions are commonly found in WMLES studies. Such grid spacings are coarser than the typical direct numerical simulation (DNS) resolutions by about a factor of ten or more. The main justification for this practice in WMLES appears to

*Senior Research Scientist, Senior Member AIAA.

†Senior Aerodynamicist, Computational AeroSciences Branch, MS 128, Fellow AIAA.

be the desire to speed up the computations given limited computing resources. However, given a particularly high Reynolds number, this approach will inevitably put too much reliance on the subgrid-scale (SGS) models to properly account for a significant range of energy-containing scales not resolved by the LES grid. Hence, there are at least two sources of error in most WMLES: the error of the particular wall model used in the near-wall region and the error coming from the coarse grid resolution used in the outer region. The outer grid resolution issue is not just limited to WMLES and applies to the wall-resolving variant of LES as well. Furthermore, there are other potential sources of numerical error that apply to both variants of LES. For example, the number of grid points across the boundary layer might be too few, particularly in regions containing a strong favorable pressure gradient. This matter is more severe for WMLES. Additionally, a relatively large time step might constitute another source of error despite allowing a numerically stable computation. The coarser grid spacings in WMLES would allow a time step larger than that in a wall-resolved calculation, wherein the near-wall grid spacing would generally dictate a relatively smaller time step. The larger time step is appealing from the point of view of minimizing the simulation run times. Insufficient span size in simulations that assume spanwise periodicity could be yet another source of error, particularly in separated flows.

Further studies are therefore needed in order to address the relevant potential sources of error for both variants of LES. A recent study performed by Rizzetta et al. [8] concerning WMLES of the NACA0012 airfoil flow with an equilibrium wall model revealed a disturbing trend and showed divergence of the WMLES predictions from the wall-resolved results as the WMLES grids were further refined along streamwise and spanwise directions while maintaining the same wall-normal grid distribution. This means that the seemingly-better result provided by the coarse-grid WMLES was fortuitous. A parametric study regarding the effect of domain span and grid resolution is carried out in the present work using wall-resolved large-eddy simulation (WRLES). This will hopefully set a precedent that will motivate the WMLES community to perform similar parametric studies, which should be feasible given the much lower computational cost of WMLES compared to WRLES.

While the NASA hump problem is a useful test case for low-speed flow separation, another problem of interest involves the shock-induced boundary layer separation observed under transonic flow conditions. This phenomenon commonly occurs in a number of practical applications where the adverse pressure gradient generated by the presence of a shock, potentially further augmented by a change in body contour, causes flow separation. The experiment by Bachalo and Johnson [9] investigates the shock-induced boundary layer separation over an axisymmetric bump that is representative of the upper surface of a transonic airfoil, as depicted in Figure 1 and reported on the NASA turbulence modeling resource website (<http://turbmodels.larc.nasa.gov> *). Despite its failure in the NASA wall hump problem, RANS with the Shear Stress Transport (SST) model was found to provide reasonable predictions in the Bachalo-Johnson flow but some differences relative to the experimental observation still remained. The better performance of the SST model in this problem is not surprising since the data from the Bachalo-Johnson experiment was used in the model calibration.

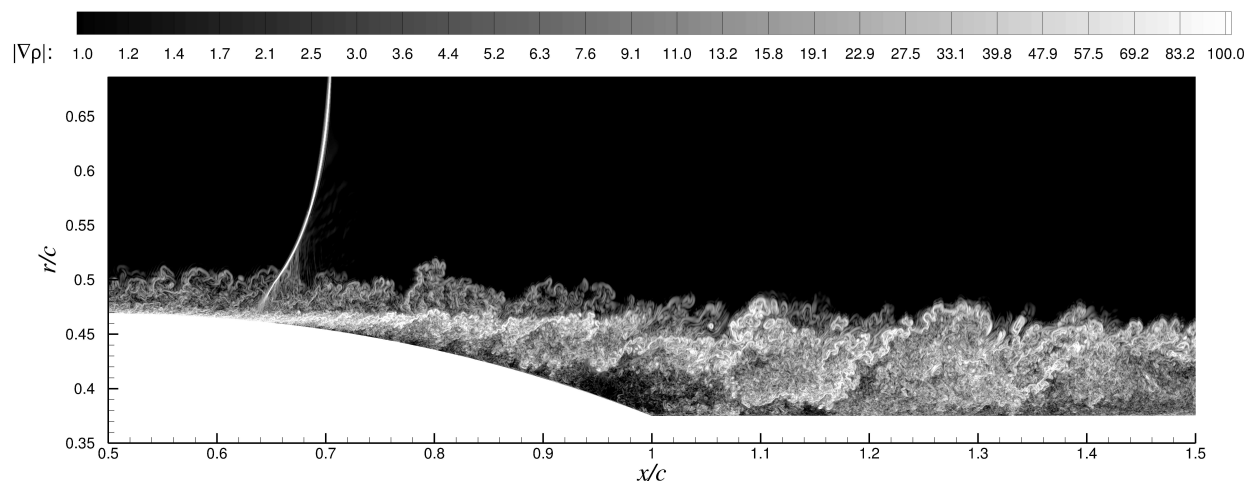


Fig. 1 Numerical schlieren (depicted in terms of normalized density gradient magnitude) visualizing shock-induced flow separation in Bachalo-Johnson flow. The axial and radial distances are scaled by the bump chord length, c . (Figure generated using simulation data from the present study.)

*Website last accessed 20 April 2018.

To our knowledge, Spalart et al. [10, 11] are the first group that used WMLES to study the Bachalo-Johnson flow. Their WMLES methodology is the same as that by Shur et al. [3], which reported good success in the NASA wall-mounted hump problem. Despite this success, the same methodology faced difficulty in correctly computing the shock location in the Bachalo-Johnson flow [10, 11]. This suggests that a particular wall model that works well under certain flow conditions may fail under different flow conditions. The incorrect prediction of the shock position by WMLES in the Bachalo-Johnson flow [10, 11] leads to incorrect flow separation and reattachment locations. Faced with the difficulty of accurately predicting the shock position in a WMLES performed using nearly 1.7 billion grid points, Spalart et al. [10, 11] had to resort to a hybrid simulation (with about 8.45 billion points) in which the attached flow region was computed using DNS while the separated region had to be simulated using improved delayed detached eddy simulation (IDDES) due to computational resource limitations. This hybrid simulation, which covered only 15 degrees of azimuth, was able to improve the shock position prediction. These observations highlight the daunting challenge associated with the prediction of separated flows and indicate that even a very large number of grid points used for a complex flow separation problem does not guarantee that the flowfield will be predicted accurately with wall-modeled approaches.

These observations coupled with the mixed success of WMLES in separated flows motivated us to embark on a systematic study exploring the use of higher-fidelity WRLES for the two benchmark problems discussed above. We have made significant strides in this regard. The results from the application of WRLES to the NASA hump model were discussed in recent papers [12, 13]. The Bachalo-Johnson problem is studied in the present paper, where we have performed wall-resolved simulations on grids containing as many as 24 billion points with a fourth-order compact finite-difference scheme. The main findings reported in this paper include the effects of azimuthal domain and grid resolution on the simulation predictions. Comparison of the computed results is made with the available experimental data. The paper is organized as follows. Section II summarizes the computational methodology employed in this study. The details of the experiment and the computational setup are discussed in sections III.A and III.B, respectively. The analysis of the simulation results are presented in section III.C. Section IV provides a summary of the findings and the concluding remarks.

II. Computational Methodology

The code used in the present study solves the unsteady three-dimensional compressible Navier-Stokes equations discretized on multiblock structured and overset grids. It employs an optimized prefactored fourth-order accurate compact finite-difference scheme [14] to compute all spatial derivatives in the governing equations. This optimized scheme offers improved dispersion characteristics compared to the standard sixth- and eighth-order compact schemes [15]. Third-order one-sided and biased schemes, respectively, are used on a boundary point and on the point next to the boundary. To eliminate the spurious high-frequency numerical oscillations that may arise from several sources (such as grid stretching, unresolved length scales and approximation of physical boundary conditions) and ensure numerical stability, we also employ high-order (up to tenth-order) compact filtering schemes [16, 17]. Instead of using an explicit SGS model, the numerical dissipation of the spatial filtering operation is chosen to serve as an implicit SGS model. The amount of numerical dissipation provided by the filter is of great concern in an implicit LES (ILES). All results presented and discussed in this paper have been obtained with the tenth-order filter, which was found to provide a minimal amount of numerical dissipation on the high-resolution grids used in the present work. Some of the early calculations were performed with the sixth-order filter, which yielded a significant amount of numerical dissipation compared to the physical turbulent dissipation on the present grids. The study of the filter effect on the predictions is deferred to a future publication.

The flow solver also has overset grid capability, which is useful in meshing complex geometries and avoiding grid point singularities. To maintain high-order accuracy throughout the entire domain, sixth-order accurate explicit Lagrangian interpolation [18] is performed whenever overset grids are used. Shock-capturing is accomplished by means of adaptive artificial dissipation [19], which is only added in the vicinity of shocks. A shock sensor, similar to that proposed by Ducros et al. [20], identifies the shock-containing regions to which adaptive artificial dissipation is applied. A Beam-Warming type approximately factorized implicit scheme with subiterations is used for the time advancement [21]. More details of the simulation methodology can be found in the publications by Uzun and coworkers [22–27].

III. Test Case: Transonic Shock-Induced Flow Separation

The problem of interest involves the shock-induced boundary layer separation over an axisymmetric bump mounted on a straight cylinder, representative of the upper surface of a transonic airfoil. A schematic of the axisymmetric bump is shown in Figure 2(a). As depicted in Figure 2(b), the axisymmetric bump is a simple circular arc of radius R_1 , which is smoothly blended to the upstream cylinder with a leading-edge fillet of radius, R_2 . Note that the radius of the circular arc, R_1 , is determined by the bump thickness, t , and the chord length, c . In the references describing the model geometry, the tangency points of the fillet are erroneously defined; hence, two potential values of R_2 could be inferred: 18.30 cm or 20.32 cm. To facilitate comparison with the results of Spalart et al. [10, 11], most of our calculations use the value chosen by them, which is $R_2 = 18.30$ cm. Because of the uncertainty in experimental model details, the potential effect of R_2 on the results is examined as part of this study by repeating our lowest grid point count case (3 billion points with 30-degree span) for a bump geometry generated with $R_2 = 20.32$ cm. Table 1 gives the dimensions of the geometric parameters that describe the bump shape used in the present study. Note that no fillet was used at the trailing edge of the bump, resulting in curvature discontinuity at that location.

Table 1 Geometric parameters of the axisymmetric bump used in the present work.

Leading-edge fillet radius, R_2	Bump chord, c	Bump thickness, t	Arc radius, R_1	Cylinder diameter, d
18.30 cm or 20.32 cm	20.32 cm	1.905 cm	$0.5(t^2 + 0.25c^2)/t$	15.24 cm

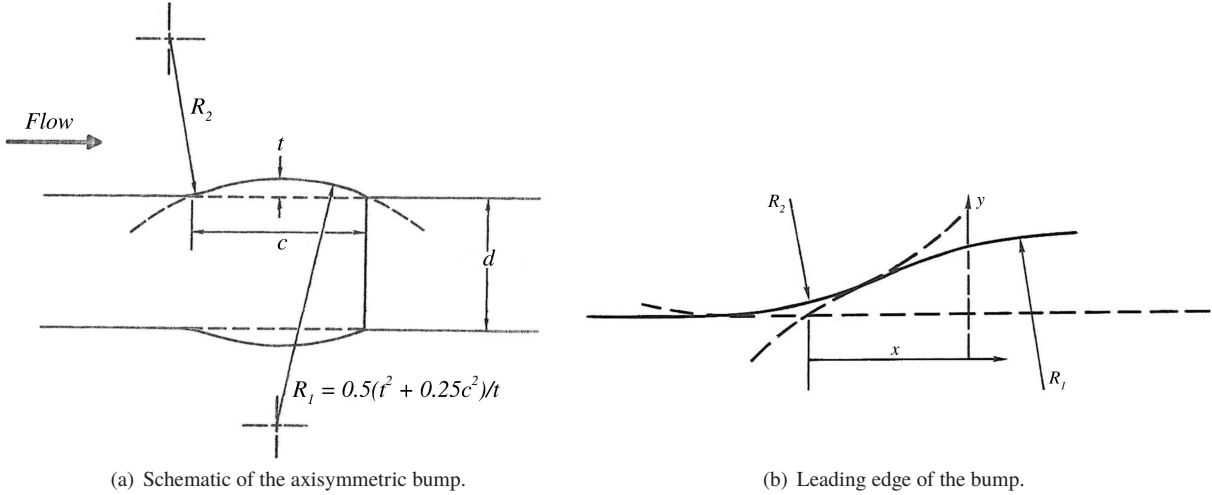
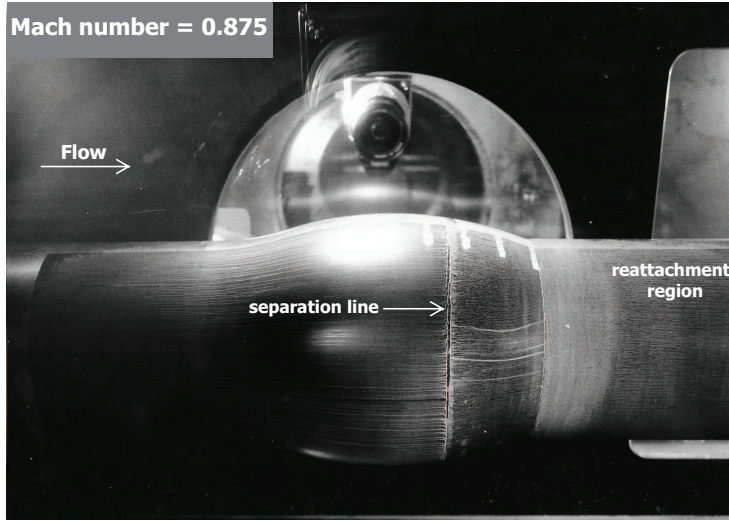


Fig. 2 Schematic of the axisymmetric bump geometry and its leading-edge details.

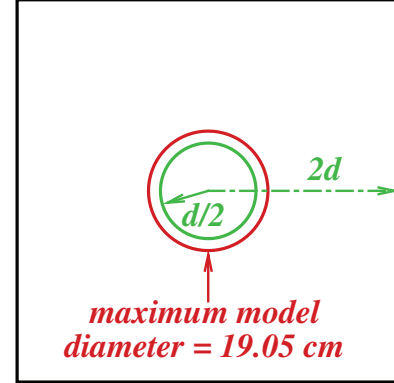
Figure 3(a) provides the experimental surface oil flow pattern obtained in the NASA Ames 2×2 ft transonic tunnel. While the surface oil flow depicts good axisymmetry in the attached region and a straight separation line that additionally confirms the axisymmetry observed until flow separation, further examination shows that there might be some azimuthal variation in the reattachment line, which is the boundary between the gray zone (depicting the separated region) and the darker zone downstream of it (depicting the reattachment region). Note that the upper and lower walls of this tunnel are porous while the other two walls are solid. Figure 3(b) provides a schematic of the experimental model within the test section. The shortest distance between the tunnel walls and the model centerline is only $2d$ or $1.5c$. Hence, the combination of the relatively small tunnel size and the “nonuniformity” of the square tunnel wall boundary conditions might have introduced some azimuthal variation in certain flow features.

The estimated boundary layer momentum-thickness Reynolds number at $1.5c$ upstream of the leading edge is $Re_\theta \approx 6600$. The freestream Mach number is 0.875. The Reynolds number based on c and the freestream velocity, u_∞ , is $Re_c = 2.763$ million. The transonic flow condition gives rise to the formation of a shock in the aft region of the bump. The interaction of this shock with the turbulent boundary layer results in boundary layer separation, which is depicted in Figure 1 based on the current simulation results. Next, we discuss the relevant details of the experiment before analyzing the simulation results.



(a) Surface oil flow pattern (courtesy of Dr. Dennis Johnson).

wind tunnel cross section
2x2 ft



$d = \text{straight cylinder diameter} = 15.24 \text{ cm}$

(b) Experimental model within the test section (drawn to scale).

Fig. 3 Bachalo-Johnson experiment in the NASA Ames 2×2 ft transonic tunnel at Mach 0.875.

A. The Bachalo-Johnson Experiment

The original experimental tests were conducted at NASA Ames in the late 1970s and led to a number of papers [9, 28–32] published in the time period of 1979 – 1987. The 1986 paper by Bachalo and Johnson [9] is generally considered to be the main reference for the problem of interest. The experimental results discussed in this paper were collected in the 2×2 ft transonic tunnel with porous upper and lower walls. Figure 2 from Bachalo and Johnson [9], reproduced here as Figure 4, gives the flow separation and reattachment in this tunnel at $x/c \approx 0.7$ and 1.1 , respectively, for a freestream Mach number of 0.875. In addition to the surface pressure and oil flow measurements, mean flowfield and Reynolds stress data were taken in the 2×2 ft tunnel experiment. Bachalo and Johnson [9] mention that the experiment was also repeated in a 6×6 ft supersonic tunnel with solid walls and both tunnel tests result in a similar surface pressure distribution. Regarding this point, page 439 of Bachalo and Johnson [9] states: *“Subsequent tests in the Ames 6×6 ft wind tunnel indicated a similar surface pressure distribution. This agreement alleviated the concern with wind tunnel wall effects on the interaction.”* However, as indicated below, this statement is not fully supported by a careful comparison of the results from the two experiments.

Some discussion of the experiment repeated in the 6×6 ft supersonic tunnel with solid walls can be found in the related publications by Horstman and Johnson [30] and Johnson [31, 32]. Only the surface pressure distribution and oil flow measurements were gathered in the 6×6 ft tunnel. Figure 3 from Horstman and Johnson [30], reproduced here as Figure 5, plots the variation of separation and reattachment locations with the freestream Mach number in the large tunnel. For the freestream Mach number of 0.875, we observe that the separation point is in the vicinity of $x/c \approx 0.66$ – 0.69 and the reattachment location is at $x/c \approx 1.17$. As noted above, for the experiment conducted in the 2×2 ft tunnel [9], the separation and reattachment locations were found to be at $x/c \approx 0.7$ and 1.1 , respectively, from the surface oil flow measurement. The separation-bubble length in the small and large tunnels is thus about $0.4c$ and 0.48 – $0.51c$, respectively. This amounts to a 20–27.5% difference in the separation-bubble length between the two facilities, which shows that there is considerable effect of the tunnel size and hence wall boundary conditions.

B. Simulation Details

The experimental Mach number and Reynolds number are exactly matched in our wall-resolved simulations. Since a wall-resolved simulation of the entire axisymmetric bump is prohibitively expensive, we consider an azimuthal portion of the axisymmetric body with periodic boundary conditions applied on the edges of the slice. A lesson learned from our previous work on the NASA wall hump problem [12, 13] was that the domain span in a spanwise-periodic calculation can have a significant effect on the growth of the separated shear layer, whose dynamics is governed by the

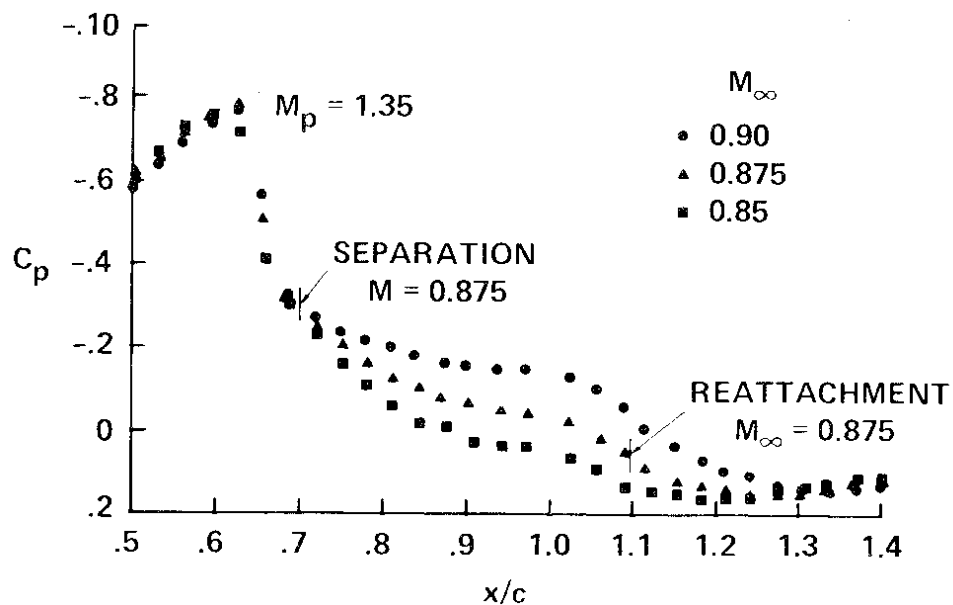


Fig. 4 Figure 2 from Bachalo and Johnson [9] showing the surface pressure data taken in the 2×2 ft tunnel at various Mach numbers.

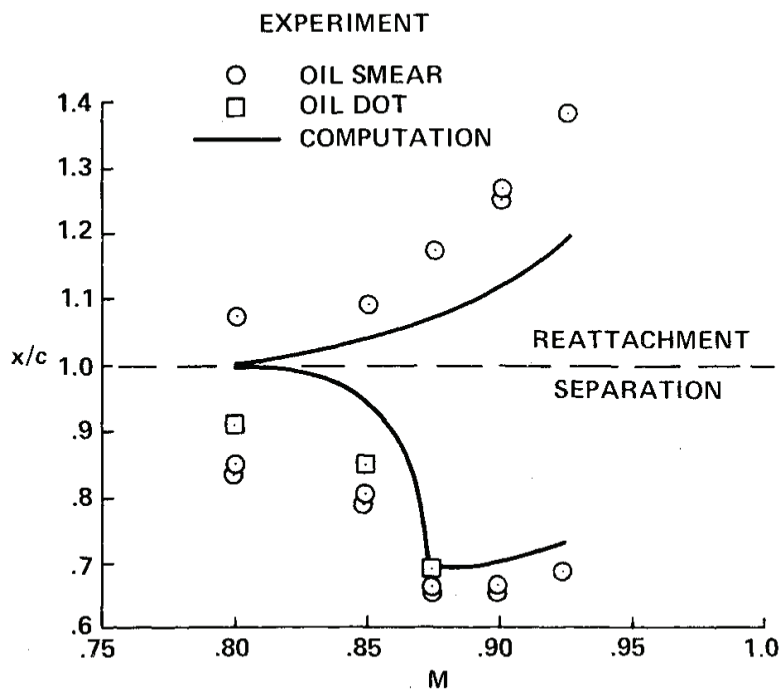


Fig. 5 Figure 3 from Horstman and Johnson [30] showing the variation of separation and reattachment locations with freestream Mach number in the 6×6 ft tunnel.

large-scale structures developing in the shear layer, and the subsequent flow reattachment location. A narrow span can constrain the growth of large structures and significantly alter the reattachment location. The effect of domain span on the numerical predictions is studied by considering 30- and 120-degree slices of the full geometry.

The differences between the small and large tunnel measurements discussed earlier were not noticed prior to initiating the computational work in this study. Because of this oversight, the tunnel wall effect was assumed negligible and therefore ignored in the simulations. In any case, only the upper and lower walls of the 2×2 ft transonic tunnel were porous and the side walls were solid. As in Spalart et al. [10, 11], who also ignored the tunnel walls, the outer boundary conditions are imposed at $r/c = 10$. Figure 6 depicts a schematic of the computational domain assuming free air and the boundary conditions applied on the domain boundaries. The leading edge of the bump geometry is at $x/c = 0$. The inflow boundary is placed at $x/c = -1.5$ while the outflow boundary is placed at $x/c = 10$. The physical domain of interest ends at $x/c = 2$. The region from $x/c = 2$ to 10 is the sponge zone, which is constructed using about 200 points with rapid grid stretching applied in the axial direction. The grid stretching in the sponge zone is augmented with additional filtering that is applied in the vicinity of the outflow boundary so that the turbulence is completely damped out before it reaches the domain exit. The outer freestream boundary is located at $r/c = 10$. Characteristic boundary conditions are imposed on the freestream and outflow boundaries. The mean flow imposed at the inflow boundary of the simulation is taken from the RANS performed by Spalart et al. [10, 11] using the SST model. The mean boundary layer thickness on the inflow boundary is $\delta_{in} \approx 0.0213c$. To reiterate, this corresponds to $Re_\theta \approx 6600$. The turbulent fluctuations imposed on the mean inflow profile are generated using a modified version of the rescaling-recycling technique, described in Uzun and Malik [13]. This inflow generation method includes several modifications proposed by Morgan et al. [33] to eliminate possible energetic low frequencies that may be artificially introduced by the recycling. The distance between the inflow and recycle planes is taken as $15 \delta_{in}$. Adiabatic viscous wall boundary conditions are imposed on the cylinder and bump surfaces.

In the small and large tunnel experiments, the shortest distance between the tunnel wall and the cylinder centerline is $1.5c$ and $4.5c$, respectively. In terms of the cylinder diameter, d , these distances correspond to $2d$ and $6d$, respectively. As the tunnel walls are positioned further away from the model in the large tunnel, the wall interference effect is presumably diminished in the large facility. We therefore expect the simulations performed in free air to be in better agreement with the measurements taken in the large tunnel. Spalart et al. [10, 11] also performed their simulations in free air with the same freestream boundary location as in the present study. This should facilitate a meaningful comparison between the two simulations. On a related note, RANS calculations by Iyer [34] showed that slip wall and characteristic farfield boundary conditions applied at $r/c = 10$ gave identical results, which suggests that tunnel walls would not have any significant effect if the experiment were to be performed in such a large tunnel.

A baseline grid, which contains 1 billion points per 10 degrees, and a refined grid, which contains 2 billion points per 10 degrees, are considered in the present study. Both grids employ a two-level overset grid strategy, depicted in Figure 7, in which the region near the wall is resolved using a fine grid and a coarser grid is used in the outer region. The overset grids communicate by means of sixth-order accurate interpolation in the overlap region. In the baseline grid, the near-wall fine grid typically extends up to $r_w^+ \approx 200$ in the attached region, where $r_w = r - r_{wall}$ is the radial distance measured from the wall (r is the radial coordinate and r_{wall} is the wall radius) and the superscript $+$ denotes wall units. The near-wall grid has a resolution of $\Delta x^+ \lesssim 30$ in the streamwise direction and $r_{wall} \Delta \theta^+ \lesssim 17.6$ in the azimuthal direction in the shock-free region. The grid clustering in the vicinity of the shock makes Δx^+ as small as 2–3 in that region. The outer region grid is coarsened by a factor of two both in the streamwise and spanwise directions. The near-wall grid contains about 100 points in the radial direction and the first grid point off the wall generally satisfies $r_w^+ \lesssim 1$. The outer grid contains about 400 grid points in the radial direction with the majority of points located within the region of turbulence-containing eddies. The grid is gradually stretched along the radial direction away from the wall. The radial grid spacing in the boundary layer edge vicinity generally satisfies $\Delta r_w^+ \lesssim 40$.

The refined grid is derived from the baseline grid. The near-wall high-resolution grid, maintained until $r_w^+ \approx 200$ in the baseline grid, is extended further away from the wall to cover the entire turbulent boundary layer and the separated region. Note that in the baseline case, the total number of radial points, split between the near-wall and outer region overset grids, is about 500. The same number of total radial points is also used in the refined case, wherein the near-wall and outer region overset grids contain about 350 and 150 points in the radial direction, respectively. The smallest grid in the present study contains 3 billion points (baseline grid with 30-degree span) and while the largest one contains 24 billion points (refined grid with 120-degree span). All calculations are run as ILES with the tenth-order filter treated as an implicit SGS model. To reiterate, the hybrid DNS-IDDES of Spalart et al. [10, 11] that we will make comparisons with, used about 8.45 billion points with a 15-degree span.

The nondimensional time step is set to $\Delta t a_\infty / c = 2.5 \times 10^{-5}$, where a_∞ is the freestream sound speed. This yields

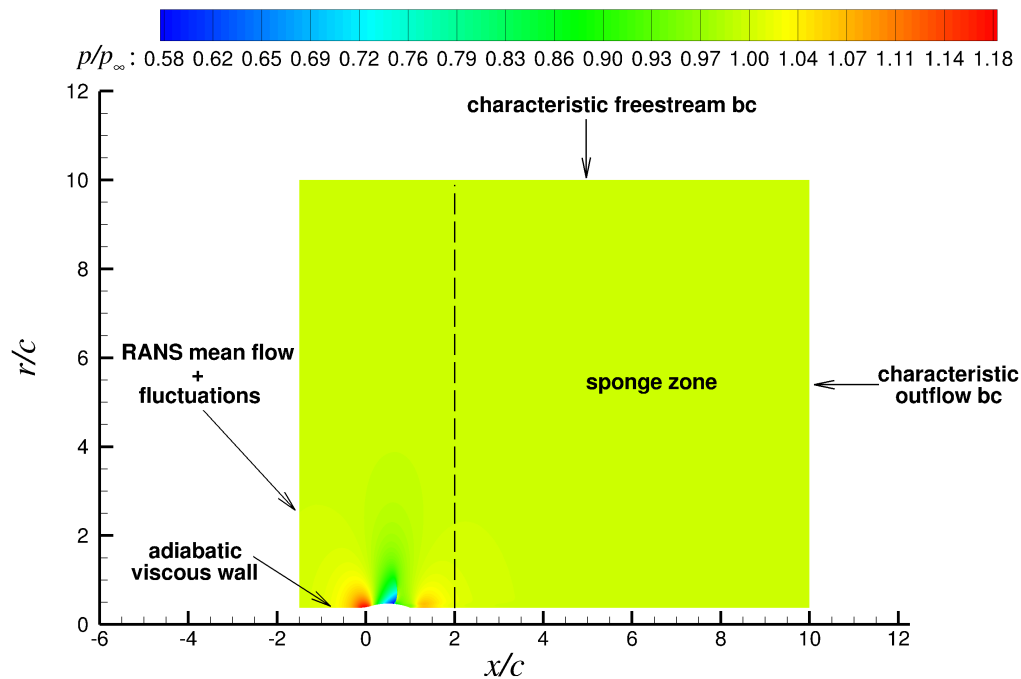


Fig. 6 Schematic of the computational domain. Contours denote the mean pressure normalized by the ambient pressure.

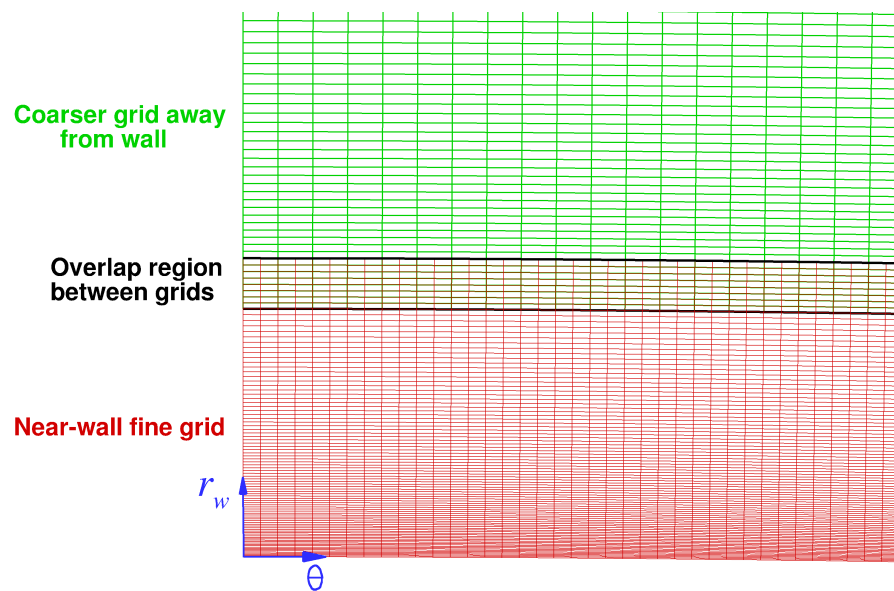


Fig. 7 Two-level overset grid system for the baseline case.

a maximum Courant-Friedrichs-Lewy (CFL) number of about 3 in the thinnest cells next to the wall. The CFL number is computed using the sum of the local mean velocity and the mean sound speed. The chosen time step corresponds to a maximum value of $\Delta t^+ \approx 0.11$ in wall units. The maximum Δt^+ is observed in the peak skin-friction region prior to flow separation. The smallest time scale in the boundary layer is found in the viscous sublayer and is $O(1)$ in wall units. The time step chosen in this study is therefore considerably smaller than the viscous time scale. The simulations are normally run for an initial period of 5 to 10 chord flow times before statistical information is gathered. One chord flow time unit, c/u_∞ , is defined as the time it takes for the freestream flow speed, u_∞ , to travel one chord length, c . Statistical data are normally gathered over 10 chord flow times unless otherwise noted. Because of the assumed mean flow axisymmetry, statistical results are averaged both in time and along the azimuthal span.

Simulations have been performed using up to 42 thousand cores on the Edison system and up to 170 thousand cores on the Cori system of the National Energy Research Scientific Computing Center (<http://www.nersc.gov>[†]). Edison contains two Intel Ivy Bridge processors (with a total of 24 cores) per node running at 2.4 GHz, while Cori contains a single Intel Knights Landing processor (with 68 cores) per node running at 1.4 GHz. The flow solver runs at approximately the same speed with the same number of nodes on both systems. On these systems, the simulation on the 24 billion point grid takes about 18–19 days to compute 10 chord flow time units.

C. Simulation Results

We now discuss the simulation results. In the following subsections, the details of the turbulent boundary layer upstream of the transonic bump are studied first. The effects of domain span, grid resolution and the bump leading-edge fillet radius on the predictions are investigated next. Other features of the flow, such as the acceleration region over the bump, surface unsteady pressure loading and the two-point azimuthal correlations upstream and downstream of flow separation, are also analyzed, and comparisons of the velocity and Reynolds stress profiles are made with the available experimental measurements. All results to be discussed have been obtained from the calculations performed with the tenth-order filter. The flow statistics have been time averaged over 10 chord flow times.

1. Properties of the Upstream Boundary Layer

We first examine the characteristics of the upstream turbulent boundary layer approaching the transonic bump. The results shown here are from our best-resolved simulation, which is the 24 billion grid case with 120-degree span. As mentioned earlier, the inflow plane in the calculation is placed at $x/c = -1.5$, where the mean flowfield profiles available from a RANS [10, 11] (with the SST model) are imposed. The turbulent fluctuations imposed on the inflow plane are generated using a rescaling-recycling technique, as mentioned earlier. Figure 8(a) shows the mean RANS velocity profile imposed on the inflow boundary and the mean velocity profiles at the axial stations of $x/c = -1$, -0.5 and -0.25 in wall units. Here, the logarithmic layer is defined as

$$U^+ = \frac{1}{\kappa} \ln(r_w^+) + C \quad (1)$$

where $r_w^+ = r_w u_\tau / \nu$, $U^+ = U/u_\tau$, $r_w (= r - r_{\text{wall}})$ is the radial wall distance (which is the same as the wall-normal distance upstream of the bump), U is the mean axial velocity, $u_\tau = \sqrt{\tau_w / \rho}$ is the friction velocity, τ_w is the wall shear stress, and ρ and ν , respectively, are the density and kinematic viscosity on the wall. The Van Driest transformation has not been applied here since Spalart et al. [10, 11] report that it only has a minor effect at the Mach number used in the simulation.

All profiles depict the expected viscous sublayer for $r_w^+ < 5$. We observe that the RANS mean profile does not have a logarithmic layer that is well represented by a von Kármán constant of $\kappa = 0.4$ – 0.41 and an intercept constant of $C = 5.0$ – 5.2 . To provide more details, the inflow boundary of the RANS [10, 11] was placed at $x/c = -13$. A slip-wall boundary condition was specified on the cylinder surface until $x/c = -3$, downstream of which a viscous wall boundary condition was applied. Perhaps the distance from $x/c = -3$ to -1.5 is not sufficient for a mean flow profile to develop in the RANS solution with the well-established logarithmic layer constants. The mean velocity profile taken from the RANS at $x/c = -1.5$ and specified at the inflow boundary is initially subjected to a relatively mild adverse pressure gradient, which becomes progressively more severe as the leading edge of the bump is approached. Figure 8(b) depicts the surface pressure coefficient variation upstream of the bump leading edge (see equation 2 for the definition of the pressure coefficient). The distance from the inflow plane to the bump leading edge is about $70 \delta_{in}$.

[†]Website last accessed 20 April 2018.

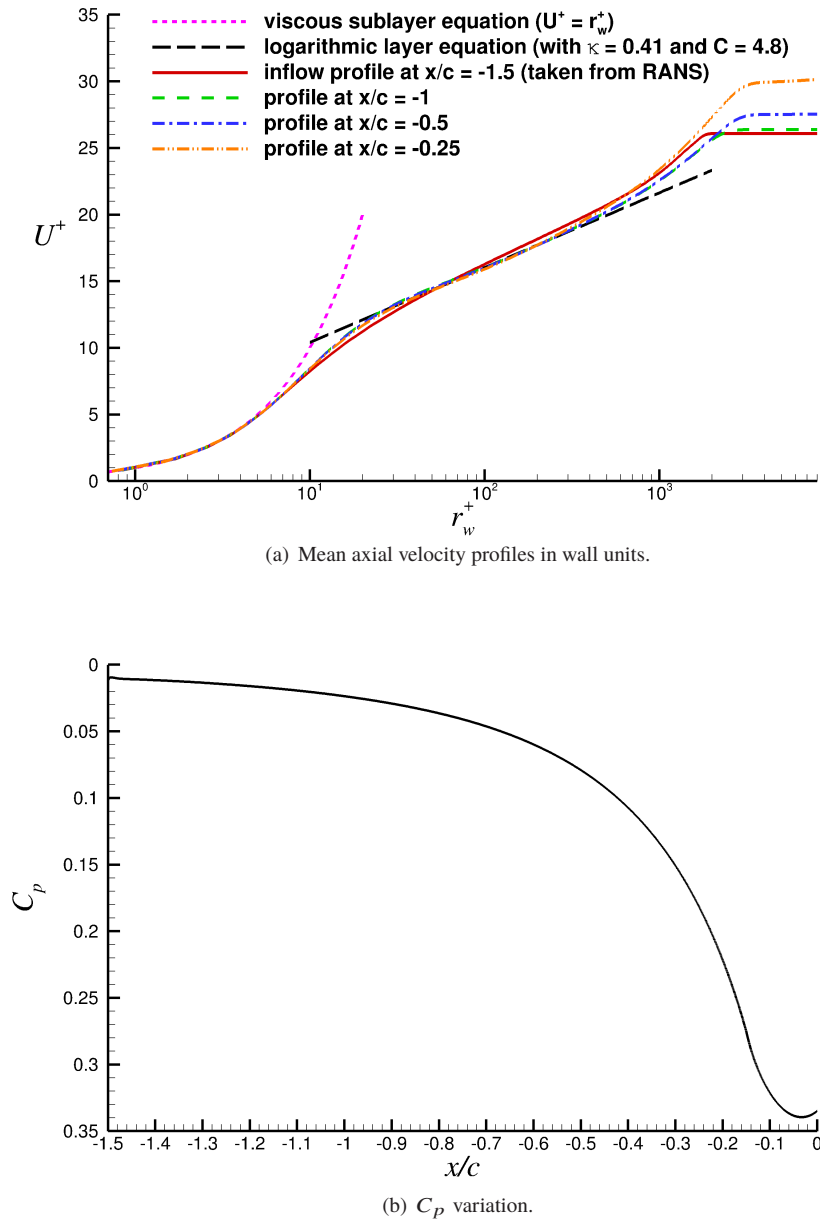


Fig. 8 Mean velocity profiles and surface pressure coefficient (C_p) variation upstream of the bump.

Previous research, such as Aubertine's review of the experimental investigations of adverse pressure-gradient boundary layers [35] as well as Coles' early survey of various turbulent boundary layers [36, 37], shows that the logarithmic law of the wall is applicable over a range of adverse pressure gradients. Hence, although the boundary layer upstream of the bump does not exactly develop under zero pressure-gradient conditions, there is reason to expect that at least the boundary layer in the mildly adverse pressure-gradient region should possess a logarithmic layer with similar properties found in its zero pressure-gradient counterpart. As seen in Figure 8(a), the downstream mean velocity profiles developing from the given RANS inflow profile under the adverse pressure-gradient conditions do indeed appear to possess a logarithmic layer that is well represented by a von Kármán constant of $\kappa = 0.41$ and an intercept constant of $C = 4.8$, which is somewhat lower than the generally established values of $C = 5.0$ – 5.2 for

zero pressure-gradient boundary layers. However, this particular intercept constant was found to be a good fit to the zero pressure-gradient boundary layer measurements of Karlsson and Johansson [38, 39]. Perhaps an incoming mean boundary layer profile with a more realistic logarithmic layer would help produce logarithmic layers better matched by a higher intercept constant of $C = 5.0$ – 5.2 in the region upstream of the bump. In spite of the questions regarding the initial RANS profile, the comparison of the predicted mean velocity profile with the experimental measurement at $x/c = -0.25$, shown in section III.C.7, depicts a reasonable agreement between the two.

Figure 9 plots the power spectral density (PSD) of the axial velocity fluctuations versus the Strouhal frequency, $Sr = fc/u_\infty$ (where f is the frequency), within the turbulent boundary layer at $x/c = -1$. This particular station is positioned within the relatively mild adverse pressure-gradient region. It is also located about $23.5 \delta_{in}$ downstream of the inflow boundary; thus, it should be a useful location to check whether the well-established hallmarks of fully-developed turbulence in a zero pressure-gradient boundary layer exist in the present case. The radial distance from the wall at this PSD location is equal to $r_w/\delta \approx 0.7$, where δ is the local boundary layer thickness. This particular wall distance is chosen so that it is not too close to the wall to be strongly influenced by the wall interference, yet it is also sufficiently away from the boundary layer edge to avoid intermittency effects. The spectrum is computed using unsteady data gathered over 10 chord flow times. It displays a typical relatively flat low-frequency range and possesses an inertial range that appears to follow Kolmogorov's $-5/3$ power scaling. A similar observation with the same inertial range scaling was also made in Klebanoff's incompressible flat-plate turbulent boundary layer spectra [40, 41] taken in the wall-distance range from 0.6δ to 0.8δ . The wall distance of $r_w/\delta \approx 0.7$, in the present case, is in the middle of this range. The inertial range in the present spectrum extends over about a decade of frequency.

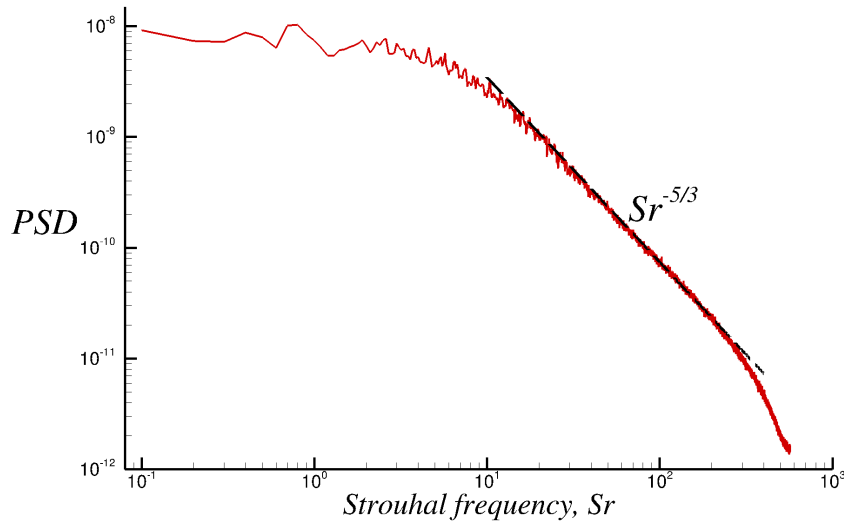


Fig. 9 PSD of the axial velocity fluctuations at $x/c = -1$ and $r_w/\delta \approx 0.7$.

Early investigations of incompressible flat-plate turbulent boundary layers [40, 41] showed that the energy decay is proportional to Sr^{-7} in the viscous dissipation range, which corresponds to the very high-frequency range of the spectrum. The high-frequency end of the present spectrum lacks such a behavior. As the present simulation is an LES and not a DNS, the high-frequency-range decay of the energy spectrum is governed by the numerical discretization and the nature of the SGS model (i.e., spatial filtering in the present ILES) rather than the physical viscous dissipation. Hence, the LES energy decay in the very high-frequency range may not reflect the physical decay. Finally, the absence of a particularly energetic discrete low frequency confirms that the turbulent inflow generation technique employed in the present study does not artificially generate spurious low-frequency motions within the boundary layer.

2. Surface Pressure and Skin-Friction Distributions

We now study the surface pressure and skin-friction distributions obtained from the two WRLES that represent the smallest and largest grid point count cases considered in the present study. The first simulation is carried out with the baseline grid resolution and an azimuthal span corresponding to a 30-degree slice of the full geometry. The second

simulation is carried out with the refined grid resolution and an azimuthal span set to 120 degrees. The details of the baseline and refined grids were provided in section III.B. The number of grid points in the two simulations is 3 and 24 billion, respectively. The leading-edge fillet radius is set to $R_2 = 18.30$ cm.

Figure 10 shows the pressure and skin-friction coefficient distributions from the two WRLES solutions and the comparison with the hybrid DNS-IDDES result of Spalart et al. [10, 11]. Experimental results from both tunnel tests, discussed earlier, are included in the pressure coefficient comparison. Two sets of large tunnel data were extracted separately from the relevant figures given in Horstman and Johnson [30] and Johnson [32]. The extracted large tunnel datasets are somewhat different from one another and we do not know the reason for this. Part of the difference may likely be the error introduced by graphically extracting the data from the two figures. Besides the shock location difference between the two tunnel tests, some scatter in the post-shock region pressure data is also present. No skin friction measurements were taken in the experiment. The pressure and skin-friction coefficients are defined as

$$C_p = \frac{p - p_\infty}{\frac{1}{2}\rho_\infty u_\infty^2} \quad \text{and} \quad C_f = \frac{\tau_w}{\frac{1}{2}\rho_\infty u_\infty^2} \quad (2)$$

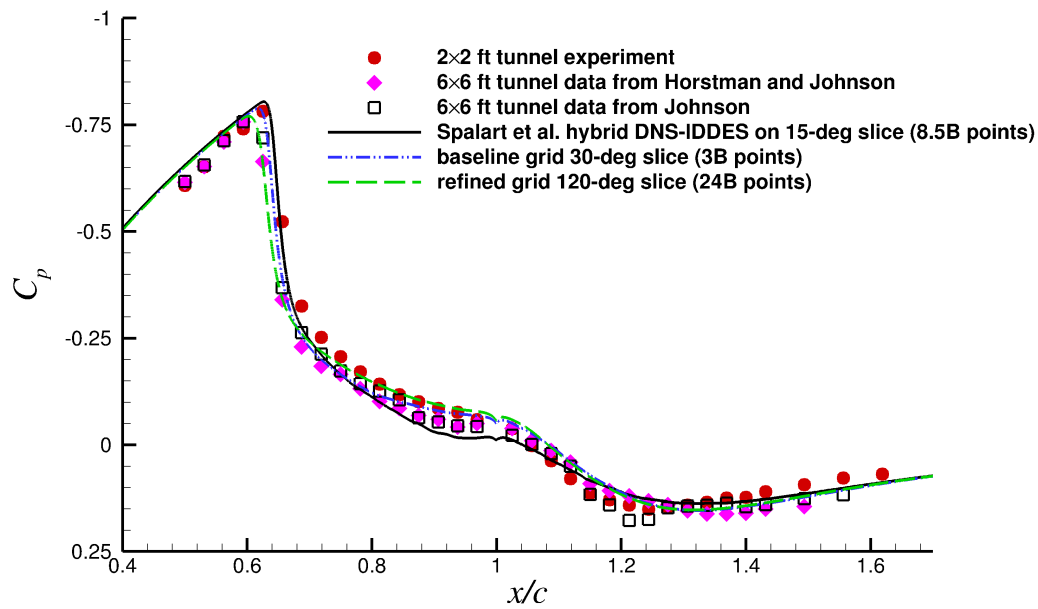
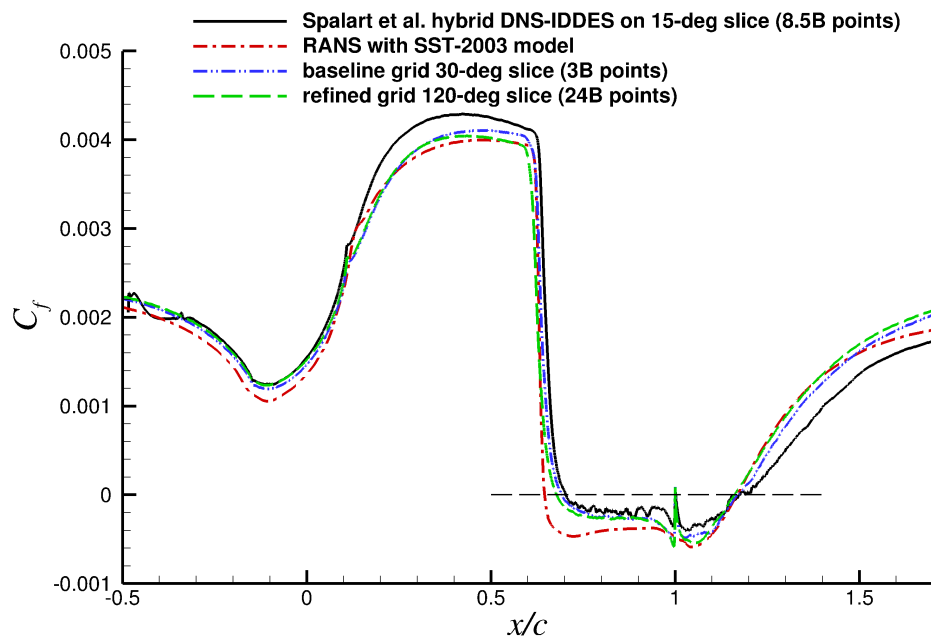
where ρ and p , respectively, are the density and pressure, τ_w is the wall shear stress and the subscript ∞ denotes the reference freestream conditions. The wall shear stress is computed from the temporally and azimuthally averaged flow.

We note that the hybrid DNS-IDDES of Spalart et al. [10, 11] performed on a 15-degree slice, was averaged over a shorter time of $2.5 c/u_\infty$. At first sight, all C_p predictions look reasonable considering the scatter present in the experimental data. As can be seen in Figure 10(a), the hybrid DNS-IDDES of Spalart et al. [10, 11] predicts a shock location similar to that observed in the 2×2 ft tunnel. Our baseline grid result shows a shock location closer to the position observed in the 6×6 ft tunnel. The refined grid result shows some more upstream shift in the shock location, which appears to be in slightly better agreement with the large tunnel observation. Such agreement of the present results with the large tunnel shock position is understandable because our simulation used characteristic freestream boundary conditions at the outer boundary that are more likely to replicate the large tunnel results. Some differences between the two WRLES predictions in the post-shock region are noticeable until around the trailing edge, after which the two predictions become nearly identical. The 24 billion point WRLES result, which is expected to be the more accurate prediction, is perhaps the best agreement that can be expected with the experiment given the difference between the simulation in free air and the wind tunnel tests and the fact that experimental uncertainties are not reported. Aside from the shock location difference between the WRLES and the hybrid DNS-IDDES, some other differences between the two are also present in the post-shock region.

Figure 10(b) shows the C_f predictions of the two WRLES solutions and the comparison with the hybrid DNS-IDDES data. The result from a RANS calculation with the SST-2003 model (which is the 2003 version of the SST model, see <http://turbmodels.larc.nasa.gov/sst.html>[‡] for more details) is also included. By extracting the axial locations at which C_f is zero, we can determine the separation and reattachment locations for each case. We see that the hybrid DNS-IDDES of Spalart et al. [10, 11] predicts the separation point at $x/c \approx 0.7$, which is the same as the separation point observed in the 2×2 ft tunnel experiment. The baseline and refined grid WRLES cases predict the separation at $x/c \approx 0.69$ and 0.68 , respectively. These agree well with the corresponding observation made in the 6×6 ft tunnel experiment, which showed the separation in the vicinity of $x/c \approx 0.66$ – 0.69 . RANS, on the other hand, is found to predict a somewhat earlier separation point at $x/c \approx 0.646$.

Between the two WRLES cases, we see very little change in the attached region C_f well upstream of separation. The effect of grid refinement is mostly felt in the peak C_f region just upstream of separation and on the separation point itself, due to the slight shift in the shock position. Minimal differences between the two cases are again observed in the reversed flow region, except that the refined grid case predicts the reattachment at $x/c \approx 1.16$, while the baseline grid case shows it at $x/c \approx 1.17$. These predictions are fairly close to the value of 1.17 observed in the 6×6 ft tunnel. This is understandable as the wind tunnel wall effects tend to diminish for the larger tunnel and our computation in free air becomes more relevant. Recall that the reattachment location in the 2×2 ft tunnel experiment was determined to be at around $x/c \approx 1.1$, which is considerably earlier than that in the larger tunnel. This difference is presumably due to the wall interference effects in the small tunnel. Due to the slight shift in the reattachment point between the two WRLES, some differences are also observed in the C_f levels downstream of the reattachment point. Both RANS and Spalart et al. [10, 11] results also show the reattachment in the vicinity of $x/c \approx 1.17$. However, the Spalart et al. [10, 11] result shows lower C_f levels in the reattachment region relative to our predictions, while the RANS result is closer to ours. All cases except the RANS also capture a small spike in C_f at the trailing edge, which is caused by

[‡]Website last accessed 20 April 2018.

(a) C_p distributions.(b) C_f distributions.**Fig. 10** Pressure coefficient (C_p) and skin-friction coefficient (C_f) comparisons.

the sharp change in curvature at the junction of the bump and cylinder surface since no fillet was used at the trailing edge. Despite the slightly different separation and reattachment point predictions between the two WRLES, both cases predict a separation-bubble length of about $0.48c$. Recall that the separation-bubble length measured in the large tunnel test is in the range of 0.48 – $0.51c$, with an “averaged” value of $0.495c$. Relative to this “averaged” value, the error in the separation-bubble length prediction of both WRLES cases is about 3%.

Another observation made from Figure 10(b) is that the peak C_f levels observed prior to flow separation are lower in the present WRLES than those in the hybrid DNS-IDDES. The RANS prediction in this region is found to be closer to the WRLES than to the DNS. The grid resolution in the attached region is clearly higher in the hybrid simulation since it employs DNS in that region. The DNS wall-normal grid spacing on the wall is about one half of that in the WRLES (note that the first grid off the wall in the WRLES still satisfies $r_w^+ < 1$), while the streamwise and spanwise resolutions of the DNS are finer than those of the WMLES by a factor of about 1.67 and 1.47, respectively. However, the time step of the DNS is nearly six times the value used in the WRLES. Both the DNS and WRLES employ a fully-implicit second-order time advancement scheme. Hence, such differences in the near-wall grid resolution and the time step could be responsible for the peak C_f differences observed here.

3. Sensitivity of C_p and C_f Distributions to Leading-Edge Fillet Radius

As noted earlier, due to the erroneous documentation of the experimental model details, the leading-edge fillet radius, R_2 , of the bump geometry has two possible values. To study the effect of R_2 , we performed calculations on two bump geometries generated with either $R_2 = 18.30$ cm or 20.32 cm. Both cases have the baseline grid resolution and an azimuthal span of 30 degrees with 3 billion points.

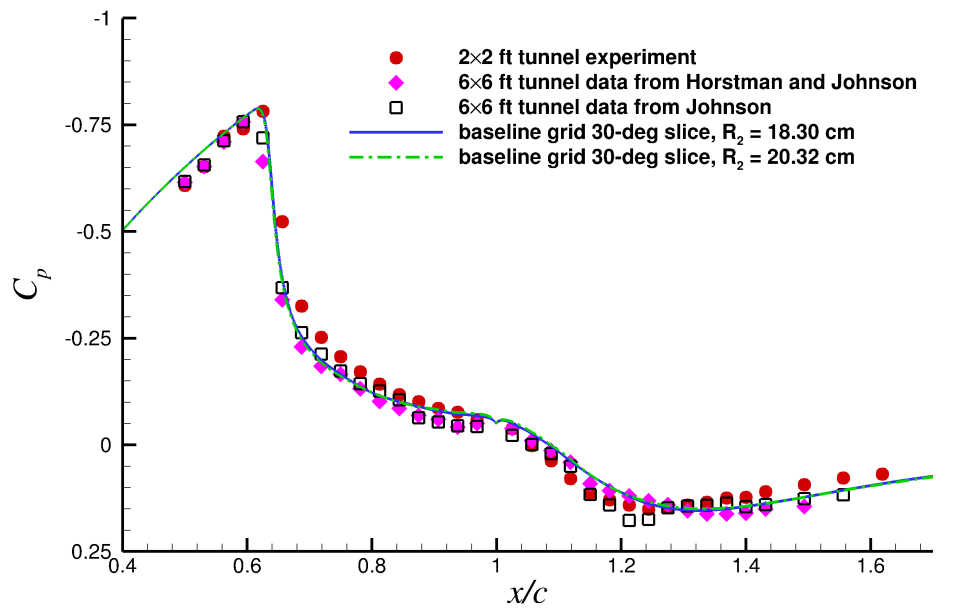
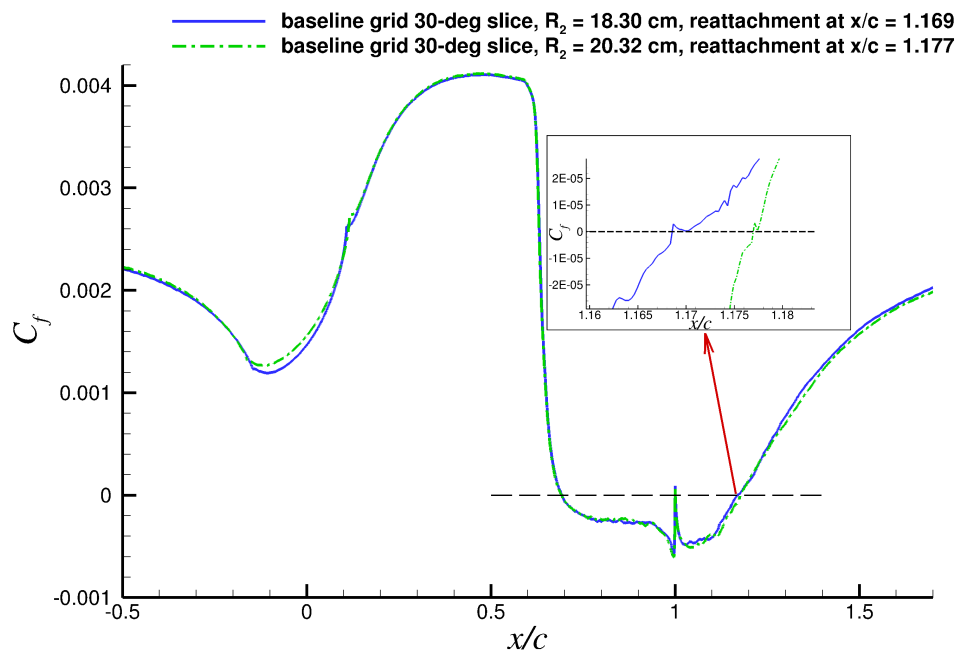
Figure 11(a) shows that the effect of R_2 on C_p in the vicinity of the shock and separation/reattachment region is rather minimal, other than the very slight upstream shift in the shock position with the larger R_2 . There are also some small C_p differences in the vicinity of the bump leading edge, which are not depicted in this figure. Figure 11(b) shows the effect of R_2 on C_f . The C_f in the vicinity of the leading edge is slightly higher with the larger R_2 , with a corresponding very slight increase in the peak C_f just upstream of separation. Despite very similar overall C_f curves between the two cases and almost identical flow separation points ($x/c \approx 0.69$), we find that the reattachment point is slightly delayed with the larger R_2 . The reattachment point moves from $x/c = 1.169$ to 1.177 between the two cases. These observations lead us to conclude that the larger R_2 value results in only slightly higher initial acceleration of the flow over the bump leading edge. This modification to the “initial conditions” of the flow developing over the leading edge then manifests its effects in the form of the differences observed in the C_p and C_f curves. As seen in the preceding subsection, the 120-degree WRLES with 24 billion points predicts the reattachment point at $x/c \approx 1.16$ with $R_2 = 18.30$ cm. We expect that with $R_2 = 20.32$ cm, the predicted reattachment point in the wide-span calculation would be closer to the experimental value of $x/c \approx 1.17$ since the larger R_2 value is found to shift the reattachment point slightly downstream. All results discussed from here onward are from the calculations performed with $R_2 = 18.30$ cm.

4. Absence of Relaminarization in the Accelerating Flow Region

A strong favorable pressure gradient, commonly found over the leading edge of airfoils, can lead to the relaminarization of an incoming turbulent boundary layer if the flow acceleration caused by the favorable pressure gradient is sufficiently high. An interesting feature of the NASA wall-mounted hump flow studied previously [12, 13] is the flow acceleration over the front portion of the hump that is strong enough to exceed the relaminarization criterion of Narasimha and Sreenivasan [42] but only over a relatively short streamwise extent. It was previously observed [13] that while the flow did not relaminarize, the turbulent skin-friction variation exhibited a plateau, also observed in the experiment of Greenblatt et al. [43], before it again began to rise.

We observe no such plateau in the C_f distribution in the case of the transonic bump. To investigate the leading-edge region of the transonic bump in more detail, Figure 12(a) plots the variation of the relaminarization parameter [42], K , for the transonic bump and compares it with the NASA wall hump. This figure reveals that the peak value in the present case is much lower than the relaminarization threshold, $K = 3 \times 10^{-6}$. To identify the reason for this, Figure 12(b) shows the C_p comparison between the two cases. We see that the NASA wall hump generates a stronger pressure gradient over the leading edge. At the same time, the chord-based Reynolds number is nearly 3 times higher for the transonic bump. The higher Reynolds number is obviously a deterrent against relaminarization. These main differences between the two cases therefore lead to a much lower peak K value in the case of the transonic bump.

Figure 13 shows the mean axial velocity profile in wall units (without the Van Driest transformation) at the transonic bump apex (i.e., at $x/c = 0.5$) from the best-resolved WRLES. Note that at the bump apex, the radial direction is

(a) C_p distributions.(b) C_f distributions.**Fig. 11** Effect of R_2 on C_p and C_f .

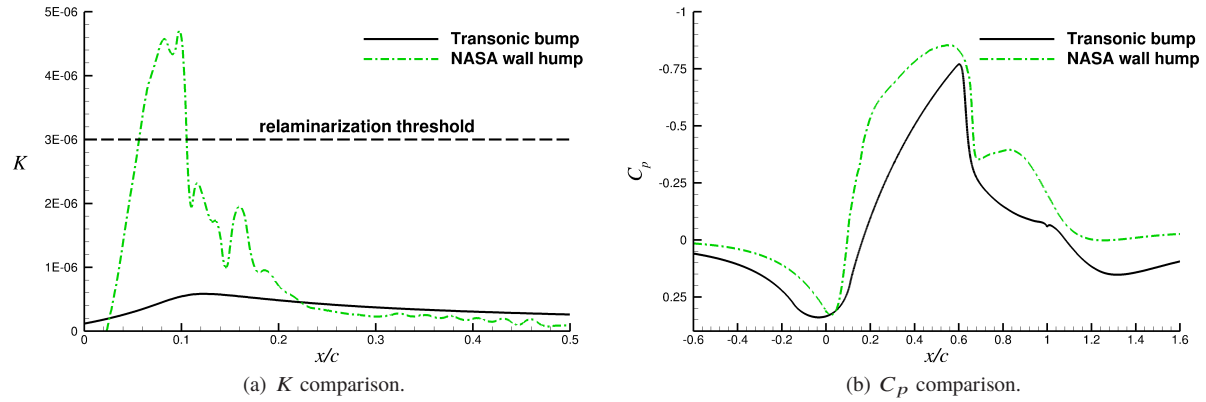


Fig. 12 Relaminarization parameter, K , and C_p comparison between the transonic bump and the NASA wall hump.

aligned with the wall-normal direction. Hence, the radial wall distance at this position is the same as the wall-normal distance. Even though the turbulent boundary layer is in an accelerating state at this particular location, the mean velocity profile appears to possess a well-defined logarithmic layer, whose constants agree with the typical values valid for zero pressure-gradient boundary layers. The hybrid DNS-IDDES of Spalart et al. [10, 11], which ran in DNS mode in the attached region, also showed the same logarithmic layer behavior at this location. Earlier studies on boundary layers subjected to favorable pressure gradients, such as the work of Fernholz and Warnack [44], reported that for very strongly-accelerated turbulent boundary layers without relaminarization, the standard logarithmic law of the wall “breaks down”. This “breakdown” can also be viewed as an upward shift of the logarithmic layer intercept constant accompanied by a reduced wall-distance range over which the law of the wall holds. For the Bachalo-Johnson flow, our mean velocity profile at the bump apex, as well as that of Spalart et al. [10, 11], does not show a “breakdown” of the logarithmic law in the accelerating region, suggesting that the favorable pressure gradient in that region is not strong enough to introduce such an effect.

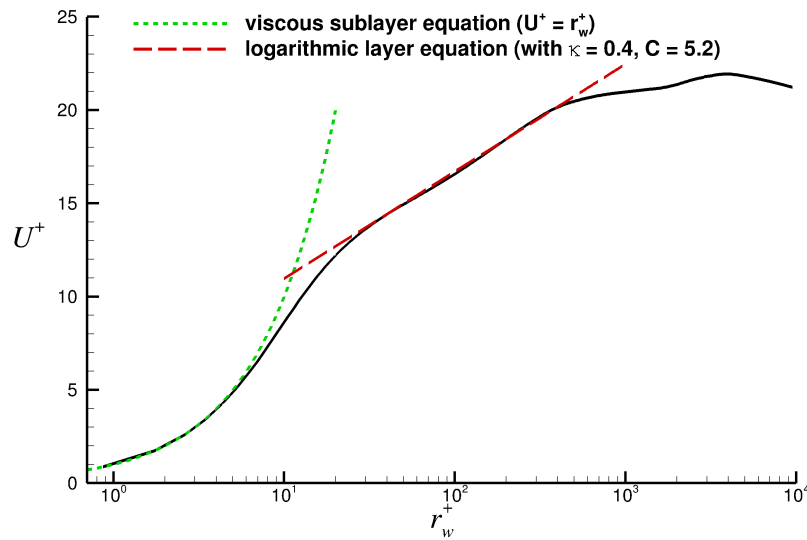


Fig. 13 Mean axial velocity profile in wall units at the transonic bump apex, $x/c = 0.5$.

At the bump apex, the best fit to the logarithmic layer is obtained with a von Kármán constant of $\kappa = 0.4$ and an intercept constant of $C = 5.2$. As discussed earlier in section III.C.1, presumably due to the “imperfections” in the incoming mean profile taken from RANS, the best fit to the logarithmic layers in the adverse pressure-gradient region upstream of the bump leading edge is obtained with $\kappa = 0.41$ and $C = 4.8$. Clearly, there is an adjustment to the logarithmic layer constants as the flow with the given RANS initial mean profile first travels through the adverse pressure-gradient region and then crosses into the favorable pressure-gradient zone. This adjustment is perhaps partly because by the time the boundary layer has reached the bump apex, it has had enough time to become independent of any imperfections in the upstream initial conditions. We should also note here that there is much debate in the literature about the universality of the von Kármán constant. There are some suggestions that the constant not only has a different value in pipes, channels and boundary layers but also has a dependence on the pressure gradient [45] and Reynolds number [46]. There is a similar lack of consensus about the value of the intercept constant. Given these issues, it is hard to reach a definitive conclusion as to why the logarithmic layer constants differ between the two zones in the present simulation. Further investigation of this subject is beyond the scope of the present paper.

5. Surface Unsteady Pressure Loading and Low-Frequency Unsteadiness

The unsteady pressure loading on the bump and downstream cylinder surfaces is examined in more detail next. Figure 14 shows the mean surface pressure and the root-mean-square (rms) surface pressure fluctuation distributions in the aft region of the bump and further downstream. These results are from the best-resolved WRLES. Upstream of the shock-containing region, the pressure unsteadiness on the surface is relatively low. The peak value of the rms pressure fluctuation approaches nearly 5% of the ambient pressure and is found within the shock-containing region at $x/c \approx 0.6272$, which is upstream of the separation point ($x/c \approx 0.68$). Visualizations of the unsteady flowfield in this region reveal some back-and-forth movement of the shock foot resulting from its interaction with the boundary layer turbulence. The surface pressure unsteadiness quickly decays post shock and maintains relatively lower values in the reversed flow region until the trailing edge, after which it starts to rise again and attains a broader secondary peak in the vicinity of the reattachment point ($x/c \approx 1.16$). The secondary peak value is about half of the primary peak. The unsteadiness then slowly decays as the reattached flow travels further downstream.

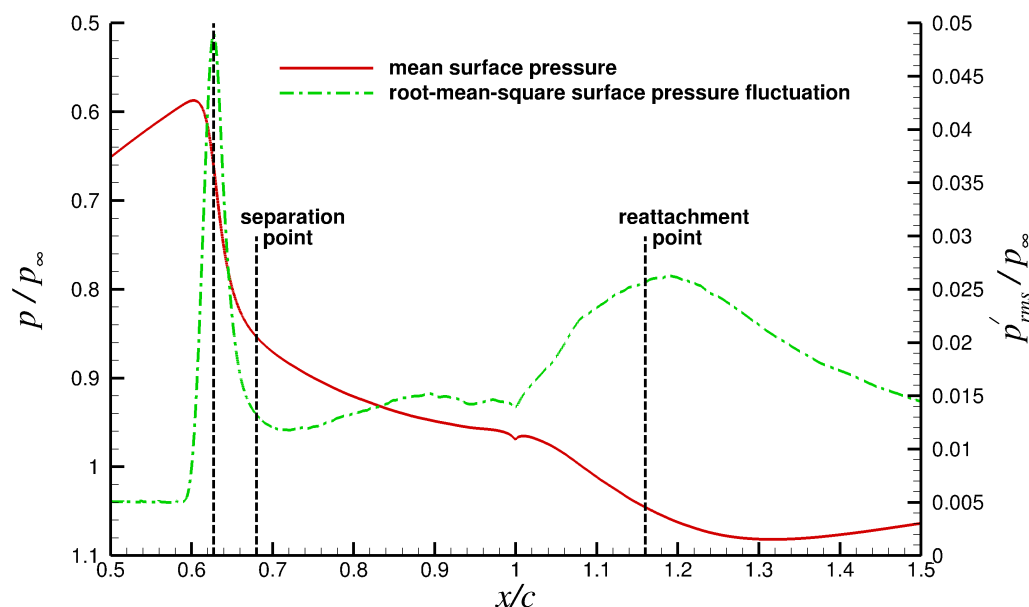


Fig. 14 Mean surface pressure and root-mean-square surface pressure fluctuation distributions.

Low-frequency unsteadiness in shock-boundary layer interactions is a well-known phenomenon even though its physical origin is still debated in the literature. The review paper by Clemens and Narayanaswamy [47] devoted to

this topic states: “A *wealth of past and recent results suggests that the unsteadiness is driven either by fluctuations in the upstream boundary layer or by some large-scale instability intrinsic to the separated flow.*” Furthermore, previous investigations of the phenomenon [48, 49] show that it is irregular and aperiodic in nature, and is composed of a broadband motion containing a range of time scales. An examination of the individual surface pressure fluctuation signals at $x/c \approx 0.6272$ (peak p_{rms}/p_∞ location) for varying azimuthal positions, as illustrated in Figure 15, reveals evidence of a low-frequency energetic motion embedded within the signals. However, the period and amplitude of the low-frequency component seems to vary from one signal to next, indicating that the phenomenon is not confined to a single low frequency. This observation concurs with the previous findings of others. We do not observe such low-frequency motions in the surface pressure fluctuation signals taken in the attached region upstream of the shock-containing region. Only a few periods of the low-frequency oscillations within the shock-containing region are captured in the current statistical sample gathered over 10 chord flow times. Hence, the primary peak of the rms surface pressure fluctuation, shown in Figure 14, may not be the fully-converged value. Unfortunately, a thorough investigation of the low-frequency unsteadiness phenomenon would require a considerably larger statistical sample, perhaps on the order of several hundred chord flow times. Given the very large grid point count of our simulations, such an exercise would obviously need very long simulation run times and is therefore prohibitively expensive at present for the current problem.

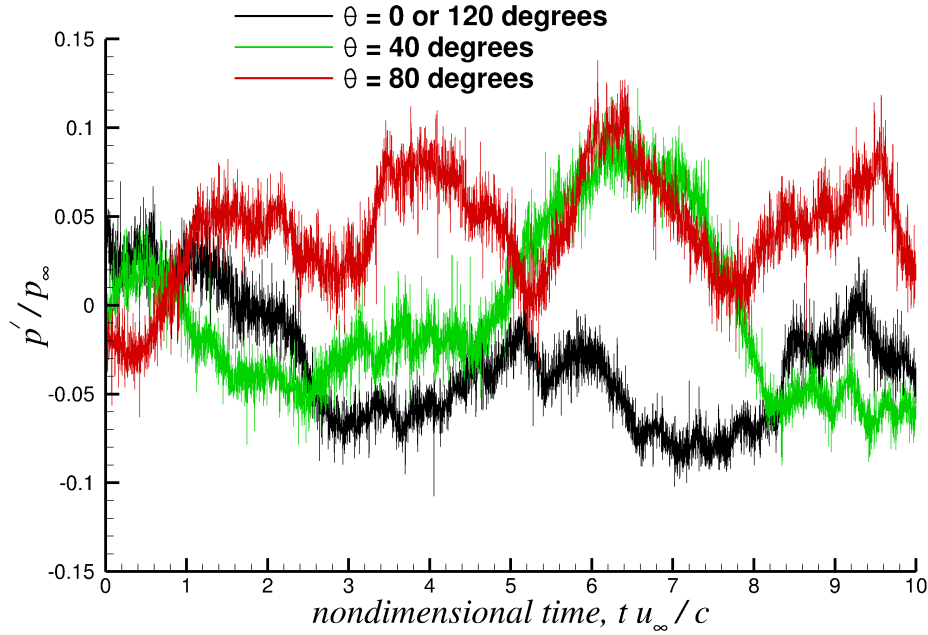


Fig. 15 Surface pressure fluctuation time history at $x/c \approx 0.6272$ for three azimuthal positions.

6. Two-Point Correlations Along the Span

Next, we examine the two-point correlations along the span at two axial stations to investigate whether a sufficiently wide span has been used in the simulations. The normalized correlations based on the axial velocity fluctuations are computed using the following expression:

$$R_{u'u'}(x, r, \Delta\theta) = \frac{\langle u'(x, r, \theta) \cdot u'(x, r, \theta + \Delta\theta) \rangle}{\langle u'(x, r, \theta) \cdot u'(x, r, \theta) \rangle} \quad (3)$$

where u' denotes the axial velocity fluctuation, $\Delta\theta$ is the azimuthal separation between the two points and the $\langle \rangle$ operator denotes averaging in time. The correlations at a given (x, r) are first computed separately for each individual azimuthal point. Note that spanwise periodicity is assumed over 120 degrees of azimuth; thus, the data is duplicated accordingly when $(\theta + \Delta\theta)$ in the above expression exceeds 120 degrees while θ is varied from 0 to 120 degrees. The

maximum value of $\Delta\theta$ is half of the azimuth or 60 degrees. All of the individual correlations are then averaged to obtain a single correlation distribution. The unsteady time history of the flowfield data gathered over 10 chord flow times from our most accurate WRLES (24 billion point grid with 120-degree slice) is used in the calculation of the correlations shown here.

Figure 16(a) shows the correlations in the attached region at $x/c = 0.5$ for various radial distances from the wall. The wall distances are normalized by the local boundary layer thickness, δ . As seen here, the correlations generally decay quickly. A longer time average should flatten the oscillatory behavior observed around zero after the initial decay. The correlations approach zero by about $\Delta\theta \approx 10$ degrees, which implies that an azimuthal span of at least 20 degrees (i.e., twice the $\Delta\theta$) is needed in the attached region. We conclude from Figure 16(a) that the chosen 120-degree azimuthal span is more than adequate in the attached region.

Figure 16(b) shows the correlations at $x/c = 1.0$, which is located within the separated flow region. As we cannot define a local boundary layer thickness in the separated region, the wall distances at this location are instead normalized by a new length scale, $d_{\text{freestream}}$, which is defined as the distance from the wall to the radial location at which the mean axial flow velocity becomes equal to the freestream velocity. We observe from this figure that the correlations at distances close to the wall approach zero by midspan (60 degrees), while the remaining ones further away from the wall do not. Figure 16(c) shows the correlations at $x/c = 1.2$, located slightly downstream of the reattachment point. The wall distances at this station are again normalized by the local boundary layer thickness since the separated flow has reattached at this location. The large structures generated in the separated shear layer region reattach without losing much of their coherence; thus, this particular station represents a reasonable location to examine the longest-range azimuthal correlations generated in the separated region. We observe from this figure that the correlations at this axial station hover around values of about -0.11 to -0.07 by the time the midspan is reached. The separated shear layer gives rise to the formation of large structures and hence the correlations in the separation/reattachment region generally decay over a larger azimuthal distance. These large structures naturally possess long time scales. Hence, the correlations in the separation/reattachment region may take a longer time interval to achieve full convergence. It therefore remains to be seen whether these correlations would approach zero by midspan with a longer time sample.

These findings also help explain why the reattachment point shifts upstream with the increased azimuthal span. The narrower azimuthal span (30-degree slice) constrains the development of large structures in the separated region, and thus affects the growth rate of the separated shear layer and its reattachment location. The observations made from Figure 16 suggest that the 120-degree azimuthal span might be barely large enough in the separated region. The 120-degree slice covers a spanwise distance in the range from $0.78540c$ to $0.98175c$. The lower bound occurs over the straight cylinder section while the upper bound is reached at the bump apex, where $x/c = 0.5$. Note that the separation-bubble length is $L_{\text{sep}} = 0.48c$; hence, these spanwise lengths correspond to about $1.64L_{\text{sep}}$ and $2.05L_{\text{sep}}$, respectively.

7. Further Comparisons with the Small Tunnel Data

We now examine the mean axial velocity profiles and Reynolds stress profiles extracted at several axial stations from the WRLES and the comparisons with the corresponding experimental measurements taken in the 2×2 ft tunnel. The computational results to be shown include the baseline grid with the 30-degree slice case (3 billion points) and the refined grid with the 120-degree slice case (24 billion points). As noted earlier, a comparison of the experimental measurements taken in the two facilities reveals that the separated flow reattaches sooner in the smaller tunnel. Because of the missing tunnel wall effects in the simulations, the comparisons to be made with the data taken in the small tunnel will only be qualitative in nature. These comparisons are shown in Figures 17 and 18. In these figures, r_w/c denotes the radial distance measured from the wall normalized by the chord, u and v are the axial and radial velocity components, respectively, and the $\langle \rangle$ operator denotes averaging in time and along the azimuthal span. The superscript $'$ on u or v denotes the velocity fluctuation.

The first axial station is located upstream of the bump leading edge, at $x/c = -0.25$, while the remaining ones are located within the separation bubble and the reattachment region. The velocity profile comparison at $x/c = -0.25$ shows reasonable agreement with the experiment and provides confidence in the upstream conditions imposed in the simulation. Both WRLES cases predict a nearly identical mean velocity profile at this station. The velocity profile comparisons at the next three axial stations, which are located within the separation bubble until $x/c = 1$, display more noticeable but modest differences between the two WRLES cases, mainly in the outer region. These profiles generally display reasonable similarity to the experiment. Recall that the WRLES cases predict earlier flow separation relative to the small tunnel experiment. This might explain why the peak velocity magnitude in the reversed

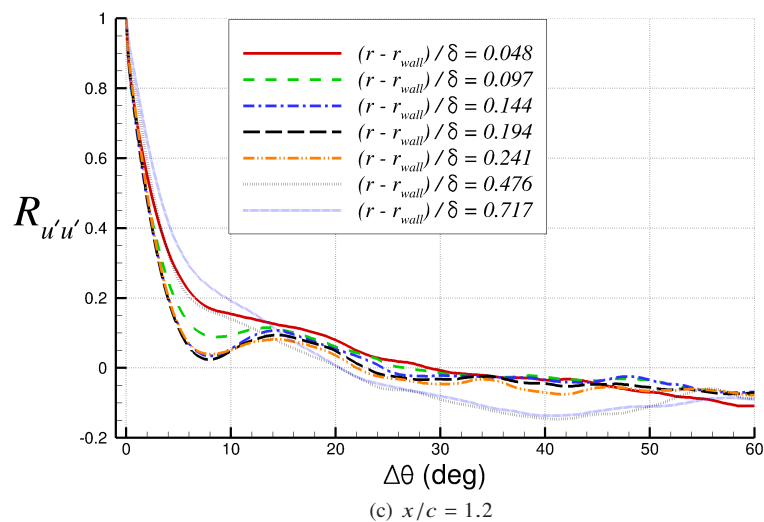
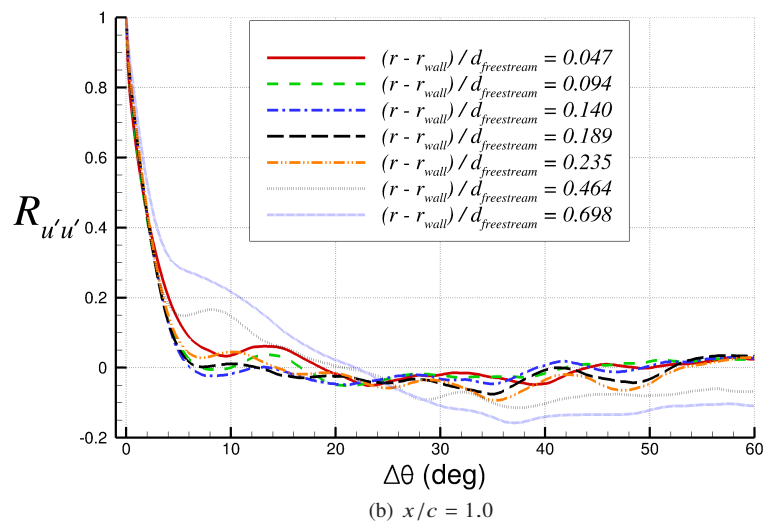
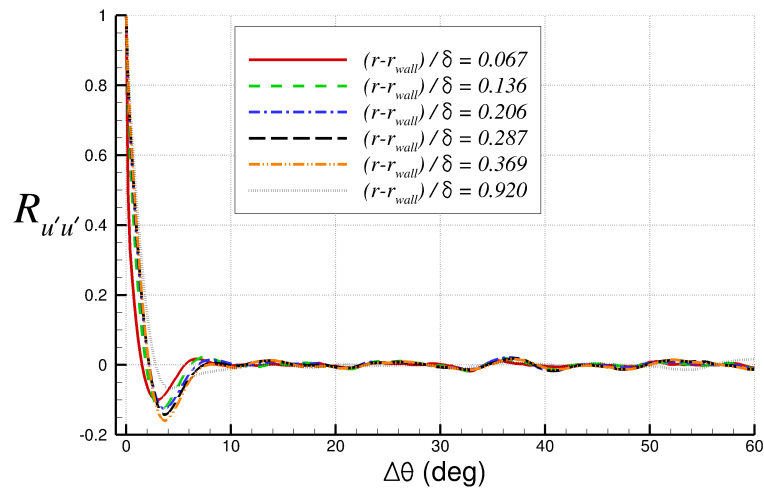


Fig. 16 Two-point correlations of axial velocity fluctuations along the azimuthal span.

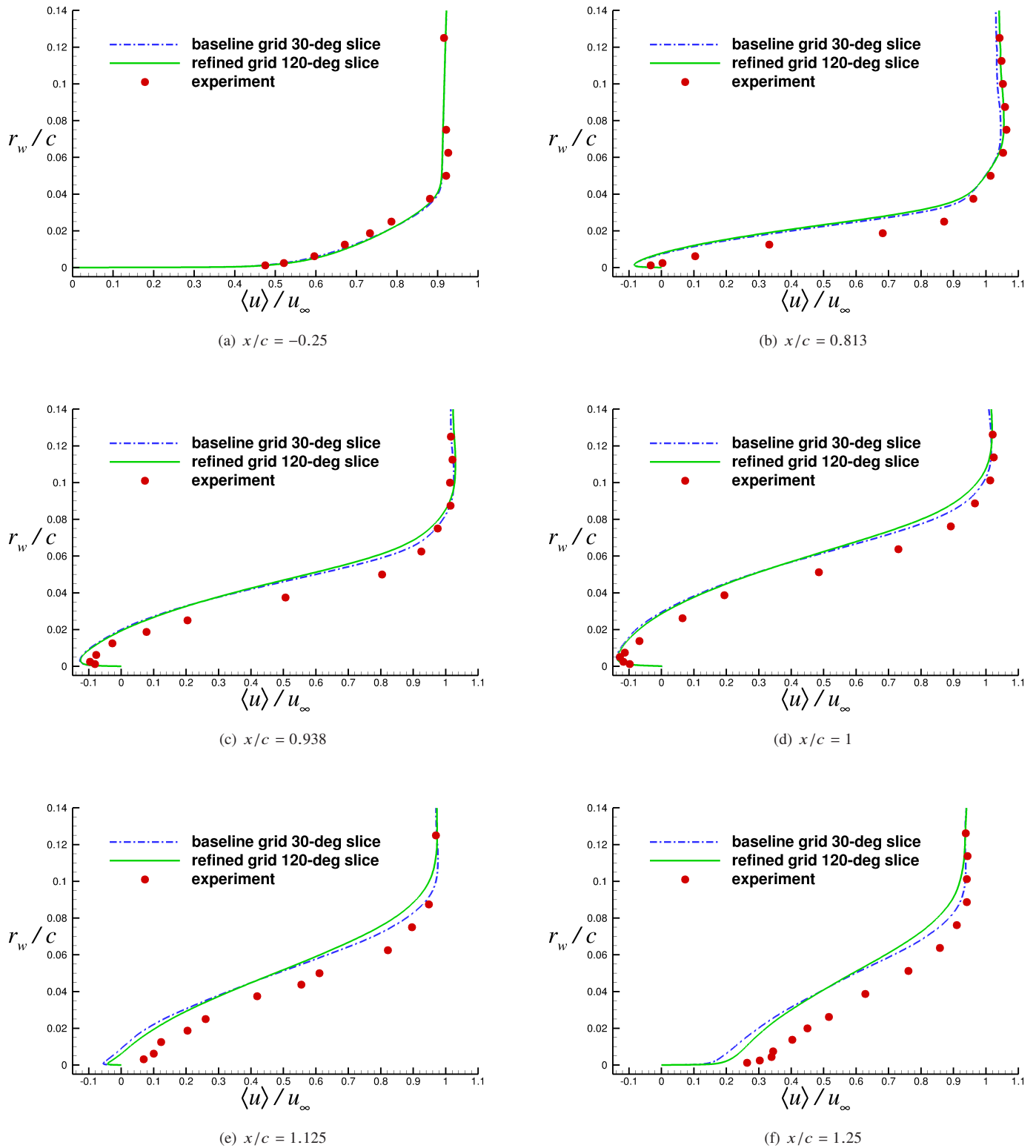


Fig. 17 Mean axial velocity profile comparisons with the measurements taken in the 2×2 ft tunnel.

flow region at $x/c = 0.813$ and 0.938 is slightly higher in the WRLES relative to the experiment. Because of the delayed reattachment in the calculations relative to the small tunnel experiment, the comparisons in the vicinity of the experimental reattachment location and downstream show greater differences relative to the experiment, as can be seen at $x/c = 1.125$ and 1.25 . At these stations, the baseline and refined WRLES profiles display greater differences between the two in the near wall region, with some differences again present in the outer region. Relative to WRLES, the earlier reattachment in the experiment gives rise to higher velocity magnitudes between the wall and the freestream at these stations.

Reynolds stress comparisons at the same axial stations, shown in Figure 18, depict generally similar qualitative behavior between the simulations and the experiment, but there are noticeable differences in the peak values at some stations. To our knowledge, there was no estimate provided for the uncertainty/error in the experimental dataset that was acquired nearly 4 decades ago. The comparison at the first station shows that the difference between the two WRLES profiles is rather minimal and provides evidence for grid convergence in the attached region well upstream of separation. Note that the velocity profile comparison at the same station also shows nearly identical results between the two WRLES cases. The grid-converged peak Reynolds stress level is about 20% lower than the peak experimental measurement at this station. The hybrid DNS-IDDES of Spalart et al. [10, 11], which ran in DNS mode in the attached region, also predicted a peak level similar to the current WRLES at this location. These observations suggest that the experimental measurement could be off or perhaps there is yet another effect in the small tunnel experiment, besides the wall interference, that is unaccounted for in the simulations.

The Reynolds stress comparisons at the other stations reveal more significant differences between the two WRLES cases in the separated and reattachment regions. As seen earlier in the two-point correlation analysis, the 120-degree span might be barely large enough for the present problem. The separated shear layer grows faster in the wide span (as demonstrated by the earlier flow reattachment relative to the narrow span) and therefore yields higher peak Reynolds stresses relative to the narrow span. The refined grid resolution of the wide-span case might also have partially contributed to the higher peak Reynolds stresses observed here. The agreement in the peak stress level between the refined wide-span case and the experiment is particularly encouraging at $x/c = 0.813$. This station represents a relatively early stage in the evolution of the separated flow. As we traverse further downstream in the separated region, the difference in the peak Reynolds stress levels between our most accurate result and the experiment becomes as much as 20%. The earlier flow reattachment in the small tunnel experiment suggests a faster growth of the separated shear layer relative to that in the simulation. The higher Reynolds stress levels observed in the experiment would correlate well with the faster shear layer growth. Both the simulation and the experiment are in the reattached flow regime by $x/c = 1.25$, where we once again see a reasonable agreement between the computed and measured peak stress levels. However, this is likely fortuitous given the delayed reattachment point in the computation. The velocity profile comparison at the same station depicts a considerable difference between the two.

IV. Conclusions

A number of wall-resolved large-eddy simulations have been performed for the Bachalo-Johnson model problem, which investigates the shock-induced boundary layer separation over an axisymmetric bump that is representative of the upper surface of a transonic airfoil. The high Reynolds number of the problem makes the wall-resolved simulations very challenging and requires billions of grid points. Simulations on grids containing as many as 24 billion points have been performed. The effects of domain span, grid resolution and the bump leading-edge fillet radius on the predictions have been examined. The larger value of the leading-edge fillet radius, R_2 , is found to slightly delay the reattachment point. Other than this effect, the C_p and C_f distributions obtained with the two possible R_2 values reveal relatively modest changes over the bump leading edge region and minor differences elsewhere. The grid resolution study between the lowest and highest grid point count cases provides evidence of grid convergence in the attached flow region well upstream of separation. The span effect is negligible in this region. However, grid refinement causes an upstream shift in the predicted shock position, which then leads to a slight upstream shift in the separation point. Furthermore, significant differences in the Reynolds stress predictions between the narrow- and wide-span cases are found in the separated region. The constrained separated shear layer in the narrow-span case generates lower levels of Reynolds stress and delays the reattachment point. The separated shear layer grows faster in the wide span and yields higher peak Reynolds stresses relative to the narrow span. The refined grid resolution of the wide-span case might also have partially contributed to the higher peak Reynolds stresses predicted in the separated region.

The two-point correlations taken along the azimuthal direction suggest that an azimuthal span of at least 20 degrees is needed in the attached region, while the 120-degree domain span might be barely large enough in the separated region.

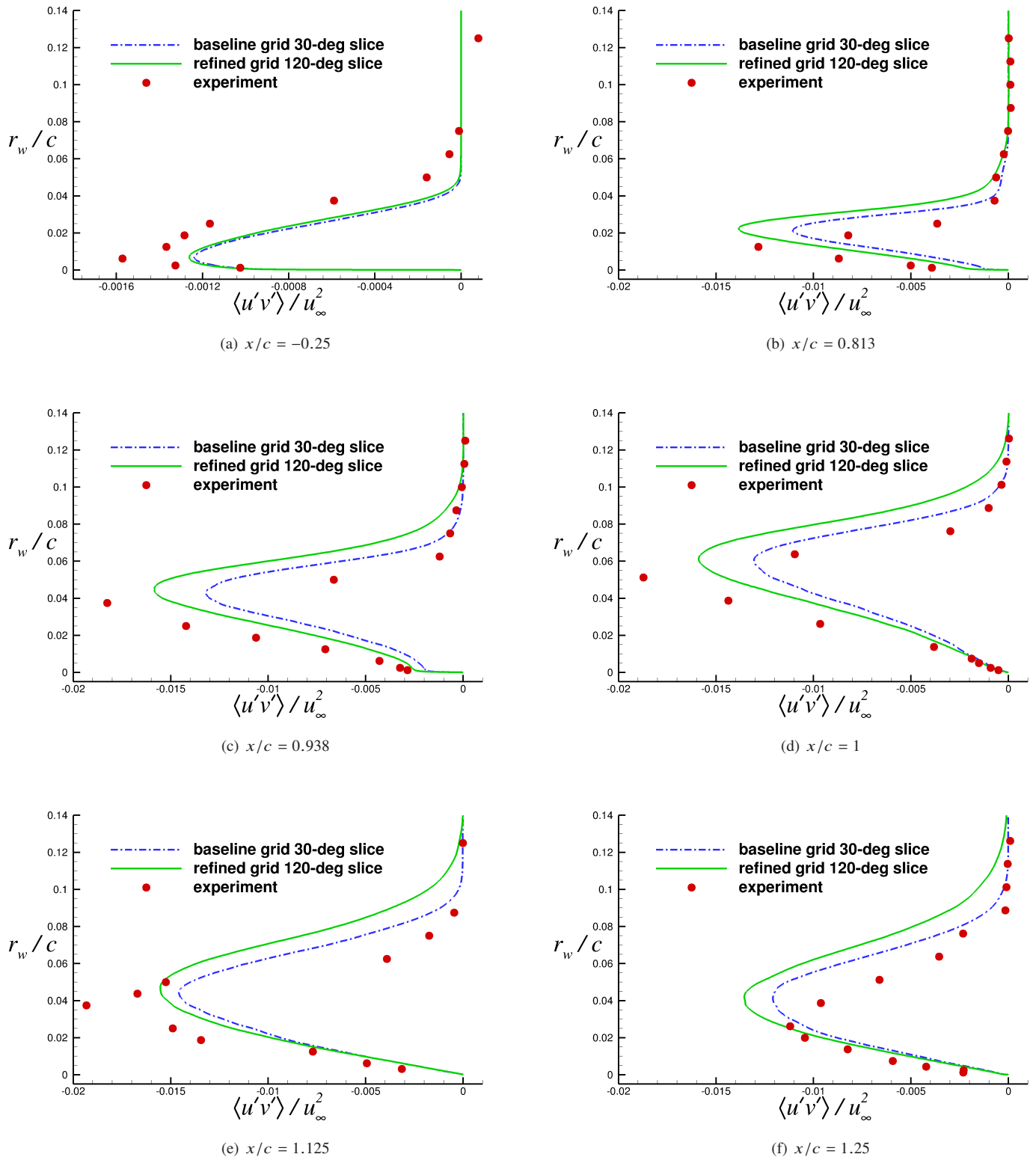


Fig. 18 Reynolds stress profile comparisons with the measurements taken in the 2×2 ft tunnel.

This is a consequence of the fact that the separated shear layer generates large-scale structures; hence, a relatively wide span is needed to resolve these structures properly. These large-scale structures possess long time scales; thus, it remains to be seen whether a longer time sample would lead to further changes in the spanwise two-point correlations within the separation/reattachment region. Depending on the behavior of the two-point correlation tails under the long-term averages, the 120-degree span may or may not be enough. Further investigation of this matter is needed.

Computed rms surface pressure fluctuations at the shock foot reach about 5 percent of ambient pressure and the level at the reattachment location drops to about half of the primary peak. An examination of the surface pressure fluctuation signals at the peak unsteady loading location for varying azimuthal positions reveals evidence of a low-frequency energetic motion embedded within the signals. However, the period and amplitude of the low-frequency component seems to vary from one signal to next, indicating that the phenomenon is not confined to a single low frequency. Only a few periods of the low-frequency oscillations within the shock-containing region are captured in the current statistical sample gathered over 10 chord flow times. Hence, the primary peak of the rms surface pressure fluctuation may not be the fully-converged value. A much larger statistical sample, perhaps as long as several hundred chord flow times, will be needed to properly investigate the low-frequency unsteadiness phenomenon.

A comparison of the experimental measurements taken in the two facilities revealed that the separated flow reattaches sooner in the smaller tunnel. This issue makes the direct comparisons with the 2×2 ft transonic tunnel measurements rather difficult as the present simulations do not model the tunnel wall effects. Nevertheless, the most accurately predicted shock position as well as flow separation and reattachment locations agree well with the limited measurements obtained separately in the 6×6 ft supersonic tunnel with solid walls. In the post-shock region, the surface pressure distribution predictions show reasonable overall agreement with the tunnel data from both tests.

Because of the issues identified in the original experiment, it is hoped that this experiment will be carefully repeated in a large facility to provide additional detailed data, including skin-friction measurement, for comparison with the computational predictions. As there is an uncertainty in the original geometry details, it is recommended that any new experimental investigation of this test case is based on the geometry used in the most accurate calculation performed in the present work (with $R_2 = 18.30$ cm) so that meaningful comparisons between the present computational study and the new experimental measurements can be made. The coordinates of the bump geometry used in this study can be made available to interested researchers. Finally, the unsteady volumetric flowfield data gathered from our best-resolved calculation (24 billion grid case with 120-degree span) generated a large dataset that is currently being probed in greater detail. The findings from this ongoing analysis will be reported in the future.

Acknowledgments

This work was sponsored by the NASA Transformational Tools and Technologies Project of the Transformative Aeronautics Concepts Program under the Aeronautics Research Mission Directorate. This research used resources of the National Energy Research Scientific Computing Center, a DOE Office of Science User Facility supported by the Office of Science of the U.S. Department of Energy under Contract No. DE-AC02-05CH11231. The access to computational resources were provided under the 2016 and 2017 DOE Advanced Scientific Computing Research Leadership Computing Challenge Programs. Some of the calculations used the computing resources provided by the NASA High-End Computing Program through the NASA Advanced Supercomputing Division at Ames Research Center. We are very grateful to Daniel Kokron for his assistance with the code optimization efforts. We acknowledge and very much appreciate useful discussions with Philippe Spalart, Michael Strelets and Dennis Johnson.

References

- [1] Rumsey, C. L., Gatski, T. B., Sellers III, W. L., Vatsa, V. N., and Viken, S. A., "Summary of the 2004 Computational Fluid Dynamics Validation Workshop on Synthetic Jets," *AIAA Journal*, Vol. 44, No. 2, 2006, pp. 194–207.
- [2] Avdis, A., Lardeau, S., and Leschziner, M., "Large Eddy Simulation of Separated Flow over a Two-Dimensional Hump with and without Control by Means of a Synthetic Slot-Jet," *Flow, Turbulence and Combustion*, Vol. 83, No. 3, 2009, pp. 343–370.
- [3] Shur, M. L., Spalart, P. R., Strelets, M. K., and Travin, A. K., "Synthetic Turbulence Generators for RANS-LES Interfaces in Zonal Simulations of Aerodynamic and Aeroacoustic Problems," *Flow, Turbulence and Combustion*, Vol. 93, No. 1, 2014, pp. 63–92.
- [4] Duda, B., and Fares, E., "Application of a Lattice-Boltzmann Method to the Separated Flow Behind the NASA Hump," *AIAA Paper 2016-1836*, January 2016.

- [5] Iyer, P. S., and Malik, M. R., "Wall-Modeled Large Eddy Simulation of Flow Over a Wall-Mounted Hump," *AIAA Paper* 2016-3186, June 2016.
- [6] Park, G. I., "Wall-Modeled Large-Eddy Simulation of a High Reynolds Number Separating and Reattaching Flow," *AIAA Journal*, Vol. 55, No. 11, 2017, pp. 3709–3721.
- [7] Probst, A., Schwaborn, D., Garbaruk, A., Guseva, E., Shur, M., Strelets, M., and Travin, A., "Evaluation of Grey Area Mitigation Tools within Zonal and Non-Zonal RANS-LES Approaches in Flows with Pressure Induced Separation," *International Journal of Heat and Fluid Flow*, Vol. 68, 2017, pp. 237–247.
- [8] Rizzetta, D. P., Garmann, D. J., and Visbal, M. R., "An Overset-Mesh Approach for Wall-Modeled LES of High-Reynolds Number Airfoil Flow," *AIAA Paper* 2018-0372, January 2018.
- [9] Bachalo, W. D., and Johnson, D. A., "Transonic, Turbulent Boundary-Layer Separation Generated on an Axisymmetric Flow Model," *AIAA Journal*, Vol. 24, No. 3, 1986, pp. 437–443.
- [10] Spalart, P., Belyaev, K., Garbaruk, A., Shur, M., Strelets, M., and Travin, A., "Large-Eddy and Direct Numerical Simulations of the Bachalo-Johnson Flow with Shock-Induced Separation," 11th International ERCOFTAC Symposium on Engineering Turbulence Modelling and Measurements, Palermo, Italy, September 2016.
- [11] Spalart, P. R., Belyaev, K. V., Garbaruk, A. V., Shur, M. L., Strelets, M. K., and Travin, A. K., "Large-Eddy and Direct Numerical Simulations of the Bachalo-Johnson Flow with Shock-Induced Separation," *Flow, Turbulence and Combustion*, Vol. 99, No. 3–4, 2017, pp. 865–885.
- [12] Uzun, A., and Malik, M. R., "Wall-Resolved Large-Eddy Simulation of Flow Separation Over NASA Wall-Mounted Hump," *AIAA Paper* 2017-0538, January 2017.
- [13] Uzun, A., and Malik, M. R., "Large-Eddy Simulation of Flow over a Wall-Mounted Hump with Separation and Reattachment," *AIAA Journal*, Vol. 56, No. 2, 2018, pp. 715–730.
- [14] Ashcroft, G., and Zhang, X., "Optimized Prefactored Compact Schemes," *Journal of Computational Physics*, Vol. 190, No. 2, 2003, pp. 459–477.
- [15] Lele, S. K., "Compact Finite Difference Schemes with Spectral-like Resolution," *Journal of Computational Physics*, Vol. 103, No. 1, 1992, pp. 16–42.
- [16] Gaitonde, D. V., and Visbal, M. R., "Padé-Type Higher-Order Boundary Filters for the Navier-Stokes Equations," *AIAA Journal*, Vol. 38, No. 11, 2000, pp. 2103–2112.
- [17] Visbal, M. R., and Gaitonde, D. V., "Very High-Order Spatially Implicit Schemes for Computational Acoustics on Curvilinear Meshes," *Journal of Computational Acoustics*, Vol. 9, No. 4, 2001, pp. 1259–1286.
- [18] Sherer, S. E., and Scott, J. N., "High-Order Compact Finite-Difference Methods on General Overset Grids," *Journal of Computational Physics*, Vol. 210, No. 2, 2005, pp. 459–496.
- [19] Kim, J. W., and Lee, D. J., "Adaptive Nonlinear Artificial Dissipation Model for Computational Aeroacoustics," *AIAA Journal*, Vol. 39, No. 5, 2001, pp. 810–818.
- [20] Ducros, F., Ferrand, V., Nicoud, F., Weber, C., Darracq, D., Gacherieu, C., and Poinsot, T., "Large-Eddy Simulation of the Shock/Turbulence Interaction," *Journal of Computational Physics*, Vol. 152, No. 2, 1999, pp. 517–549.
- [21] Ekaterinaris, J. A., "Implicit, High-Resolution, Compact Schemes for Gas Dynamics and Aeroacoustics," *Journal of Computational Physics*, Vol. 156, No. 2, 1999, pp. 272–299.
- [22] Uzun, A., and Hussaini, M. Y., "Investigation of High Frequency Noise Generation in the Near-Nozzle Region of a Jet Using Large Eddy Simulation," *Theoretical and Computational Fluid Dynamics*, Vol. 21, No. 4, 2007, pp. 291–321.
- [23] Uzun, A., and Hussaini, M. Y., "Simulation of Noise Generation in Near-Nozzle Region of a Chevron Nozzle Jet," *AIAA Journal*, Vol. 47, No. 8, 2009, pp. 1793–1810.
- [24] Uzun, A., Bin, J., and Hussaini, M. Y., "High-Fidelity Numerical Simulation of a Chevron Nozzle Jet Flow," *International Journal of Aeroacoustics*, Vol. 10, No. 5&6, 2011, pp. 531–564.
- [25] Uzun, A., and Hussaini, M. Y., "Prediction of Noise Generated by a Round Nozzle Jet Flow Using Computational Aeroacoustics," *Journal of Computational Acoustics*, Vol. 19, No. 3, 2011, pp. 291–316.

- [26] Uzun, A., Hussaini, M. Y., and Streett, C. L., "Large-Eddy Simulation of a Wing Tip Vortex on Overset Grids," *AIAA Journal*, Vol. 44, No. 6, 2006, pp. 1229–1242.
- [27] Uzun, A., Kumar, R., Hussaini, M. Y., and Alvi, F. S., "Simulation of Tonal Noise Generation by Supersonic Impinging Jets," *AIAA Journal*, Vol. 51, No. 7, 2013, pp. 1593–1611.
- [28] Bachalo, W. D., and Johnson, D. A., "An Investigation of Transonic Turbulent Boundary Layer Separation Generated on an Axisymmetric Flow Model," AIAA Paper 79-1479, July 1979.
- [29] Johnson, D. A., Hortsman, C. C., and Bachalo, W. D., "Comparison Between Experiment and Prediction for a Transonic Turbulent Separated Flow," *AIAA Journal*, Vol. 20, No. 6, 1982, pp. 737–744.
- [30] Horstman, C. C., and Johnson, D. A., "Prediction of Transonic Separated Flows," *AIAA Journal*, Vol. 22, No. 7, 1984, pp. 1001–1003.
- [31] Johnson, D. A., "Predictions of Transonic Separated Flow with an Eddy-Viscosity/Reynolds-Shear-Stress Closure Model," AIAA Paper 85-1683, July 1985.
- [32] Johnson, D. A., "Transonic Separated Flow Predictions with an Eddy-Viscosity/Reynolds-Stress Closure Model," *AIAA Journal*, Vol. 25, No. 2, 1987, pp. 252–259.
- [33] Morgan, B., Larsson, J., Kawai, S., and Lele, S. K., "Improving Low-Frequency Characteristics of Recycling/Rescaling Inflow Turbulence Generation," *AIAA Journal*, Vol. 49, No. 3, 2011, pp. 582–597.
- [34] Iyer, P. S., Private Communication, June 2017.
- [35] Aubertine, C. D., "Reynolds Number Effects on an Adverse Pressure Gradient Turbulent Boundary Layer," Ph.D. thesis, Stanford University, Stanford, California, 2005.
- [36] Coles, D., "The Law of the Wake in the Turbulent Boundary Layer," *Journal of Fluid Mechanics*, Vol. 1, No. 2, 1956, pp. 191–226.
- [37] Coles, D. E., "Turbulent Boundary Layers in Pressure Gradients: A Survey Lecture Prepared for the 1968 AFOSR-IFP – Stanford Conference on Computation of Turbulent Boundary Layers," RAND Corporation, RM-6142-PR, Santa Monica, California. As of April 17, 2018: https://www.rand.org/pubs/research_memoranda/RM6142.html, October 1969.
- [38] Karlsson, R., and Johansson, T. G., "LDV Measurements of Higher Order Moments of Velocity Fluctuations in a Turbulent Boundary Layer," *Laser Anemometry in Fluid Mechanics III: Selected Papers from the Third International Symposium on Applications of Laser Anemometry to Fluid Mechanics*, edited by R. J. Adrian, T. Asanuma, D. F. G. Durao, F. Durst and J. H. Whitelaw, Ladoan-Instituto Superior Technico, Portugal, 1988, pp. 273–289.
- [39] So, R. M. C., Zhang, H. S., Gatski, T. B., and Speziale, C. G., "Logarithmic Laws for Compressible Turbulent Boundary Layers," *AIAA Journal*, Vol. 32, No. 11, 1994, pp. 2162–2168.
- [40] Klebanoff, P. S., "Characteristics of Turbulence in a Boundary Layer with Zero Pressure Gradient," NACA Report 1247, 1955.
- [41] Schlichting, H., *Boundary-Layer Theory, Seventh Edition*, McGraw-Hill Book Company, 1979, pp. 569–570.
- [42] Narasimha, R., and Sreenivasan, K. R., "Relaminarization in Highly Accelerated Turbulent Boundary Layers," *Journal of Fluid Mechanics*, Vol. 61, 1973, pp. 417–447.
- [43] Greenblatt, D., Paschal, K. B., Yao, C.-S., Harris, J., Schaeffler, N. W., and Washburn, A. E., "A Separation Control CFD Validation Test Case, Part 1: Baseline and Steady Suction," *AIAA Journal*, Vol. 44, No. 12, 2006, pp. 2820–2830.
- [44] Fernholz, H. H., and Warnack, D., "The Effects of a Favourable Pressure Gradient and of the Reynolds Number on an Incompressible Axisymmetric Turbulent Boundary Layer. Part 1. The Turbulent Boundary Layer," *Journal of Fluid Mechanics*, Vol. 359, 1998, pp. 329–356.
- [45] Nagib, H. M., and Chauhan, K. A., "Variations of von Kármán Coefficient in Canonical Flows," *Physics of Fluids*, Vol. 20, No. 10, 2008, p. 101518.
- [46] Wosnik, M., Castillo, L., and George, W. K., "A Theory for Turbulent Pipe and Channel Flows," *Journal of Fluid Mechanics*, Vol. 421, 2000, pp. 115–145.

- [47] Clemens, N. T., and Narayanaswamy, V., “Low-Frequency Unsteadiness of Shock Wave/Turbulent Boundary Layer Interactions,” *Annual Review of Fluid Mechanics*, Vol. 46, 2014, pp. 469–492.
- [48] Dussauge, J.-P., Dupont, P., and Debiève, J.-F., “Unsteadiness in Shock Wave Boundary Layer Interactions with Separation,” *Aerospace Science and Technology*, Vol. 10, No. 2, 2006, pp. 85–91.
- [49] Priebe, S., and Martin, M. P., “Low-Frequency Unsteadiness in Shock Wave–Turbulent Boundary Layer Interaction,” *Journal of Fluid Mechanics*, Vol. 699, 2012, pp. 1–49.